



**NAVAL  
POSTGRADUATE  
SCHOOL**

**MONTEREY, CALIFORNIA**

**THESIS**

**INTEGRATION AND CONTROL OF A BATTERY  
BALANCING SYSTEM**

by

Peter L. Norgaard

December 2013

Thesis Advisor:  
Second Reader:

Alexander L. Julian  
Giovanna Oriti

**Approved for public release; distribution is unlimited**

THIS PAGE INTENTIONALLY LEFT BLANK

**REPORT DOCUMENTATION PAGE**
*Form Approved OMB No. 0704-0188*

Public reporting burden for this collection of information is estimated to average 1 hour per response, including the time for reviewing instruction, searching existing data sources, gathering and maintaining the data needed, and completing and reviewing the collection of information. Send comments regarding this burden estimate or any other aspect of this collection of information, including suggestions for reducing this burden, to Washington Headquarters Services, Directorate for Information Operations and Reports, 1215 Jefferson Davis Highway, Suite 1204, Arlington, VA 22202-4302, and to the Office of Management and Budget, Paperwork Reduction Project (0704-0188) Washington, DC 20503.

|   |  |  |
|---|--|--|
| <b>1. AGENCY USE ONLY (Leave blank)</b>   | <b>2. REPORT DATE</b><br>December 2013 | <b>3. REPORT TYPE AND DATES COVERED</b><br>Master's Thesis |
| <b>4. TITLE AND SUBTITLE</b><br>INTEGRATION AND CONTROL OF A BATTERY BALANCING SYSTEM   |  | <b>5. FUNDING NUMBERS</b>                                  |
| <b>6. AUTHOR(S)</b> Peter L. Norgaard   |  |  |
| <b>7. PERFORMING ORGANIZATION NAME(S) AND ADDRESS(ES)</b><br>Naval Postgraduate School<br>Monterey, CA 93943-5000   |  | <b>8. PERFORMING ORGANIZATION REPORT NUMBER</b>            |
| <b>9. SPONSORING /MONITORING AGENCY NAME(S) AND ADDRESS(ES)</b><br>N/A  |  | <b>10. SPONSORING/MONITORING AGENCY REPORT NUMBER</b>      |
| <b>11. SUPPLEMENTARY NOTES</b> The views expressed in this thesis are those of the author and do not reflect the official policy or position of the Department of Defense or the U.S. Government. IRB Protocol number ____ N/A ____.  |  |  |
| <b>12a. DISTRIBUTION / AVAILABILITY STATEMENT</b><br>Approved for public release; distribution is unlimited   |  | <b>12b. DISTRIBUTION CODE</b><br>A                         |
| <b>13. ABSTRACT (maximum 200 words)</b><br>The primary focus of this research was the integration of series-loaded resonant (SLR) converters into a field-programmable gate array controlled power converter for use in balancing a series-connected battery bank. As the limits of the power grid are continually extended, the market demand for alternate power sources and energy storage systems will continue to grow. The goal of this research was to build and integrate a bank of SLR converters for use in balancing a series-connected battery bank that is part of a broader system used for power storage and conversion. Voltage and temperature sensors were used to monitor individual cell state-of-charge and rate-of-charge and discharge. Voltage-to-frequency conversion was used to read sensor parameters. A battery balancing algorithm was designed, integrated and demonstrated with experimental results. |  |  |

**14. SUBJECT TERMS** power storage, series loaded resonant converter, voltage calibration, temperature sensing, battery balancing, field programmable gate array

**15. NUMBER OF PAGES**  
97

**16. PRICE CODE**
**17. SECURITY CLASSIFICATION OF REPORT**  
Unclassified

**18. SECURITY CLASSIFICATION OF THIS PAGE**  
Unclassified

**19. SECURITY CLASSIFICATION OF ABSTRACT**  
Unclassified

**20. LIMITATION OF ABSTRACT**  
UU

THIS PAGE INTENTIONALLY LEFT BLANK

**Approved for public release; distribution is unlimited**

**INTEGRATION AND CONTROL OF A BATTERY BALANCING SYSTEM**

Peter L. Norgaard  
Lieutenant, United States Navy  
B.S., The United States Merchant Marine Academy, 2004

Submitted in partial fulfillment of the  
requirements for the degree of

**MASTER OF SCIENCE IN ELECTRICAL ENGINEERING**

from the

**NAVAL POSTGRADUATE SCHOOL**  
**December 2013**

Author: Peter L. Norgaard

Approved by: Alexander L. Julian  
Thesis Advisor

Giovanna Oriti  
Second Reader

R. Clark Robertson  
Chairman, Department of Electrical and Computer Engineering

THIS PAGE INTENTIONALLY LEFT BLANK

## **ABSTRACT**

The primary focus of this research was the integration of series-loaded resonant (SLR) converters into a field-programmable gate array controlled power converter for use in balancing a series-connected battery bank. As the limits of the power grid are continually extended, the market demand for alternate power sources and energy storage systems will continue to grow. The goal of this research was to build and integrate a bank of SLR converters for use in balancing a series-connected battery bank that is part of a broader system used for power storage and conversion. Voltage and temperature sensors were used to monitor individual cell state-of-charge and rate-of-charge and discharge. Voltage-to-frequency conversion was used to read sensor parameters. A battery balancing algorithm was designed, integrated and demonstrated with experimental results.

THIS PAGE INTENTIONALLY LEFT BLANK

## TABLE OF CONTENTS

|      |   |    |
|------|---|----|
| I.   | INTRODUCTION.....   | 1  |
| A.   | BACKGROUND .....  | 1  |
| B.   | ENERGY STORAGE.....   | 2  |
| C.   | ENERGY CONVERSION .....   | 6  |
| D.   | BATTERY BALANCING.....  | 11 |
| II.  | ANALOG-TO-DIGITAL CONVERSION AND PROCESSING .....                         | 15 |
| A.   | OPERATION OF THE PRECISION VOLTAGE-TO-FREQUENCY<br>CONVERTER (LM231)..... | 15 |
| B.   | MEASURING THE SIGNAL OUTPUT .....   | 18 |
| C.   | CALIBRATION RESULTS.....  | 19 |
| D.   | READING THE DIGITAL DATA.....   | 26 |
| III. | DESIGN OF THE BATTERY BALANCING CONTROL ALGORITHM .....                   | 35 |
| A.   | BACKGROUND .....  | 35 |
| B.   | DESIGNING THE BATTERY BALANCING ALGORITHM.....                            | 36 |
| IV.  | CONCLUSIONS AND RECOMMENDATIONS.....                                      | 43 |
| A.   | OBSERVATIONS AND FUTURE WORK.....   | 43 |
| B.   | CONCLUSION .....  | 43 |
|      | APPENDIX A. BATTERY BALANCING ALGORITHM .....                             | 45 |
|      | APPENDIX B. INITIAL CONDITIONS FILE .....                                 | 47 |
|      | APPENDIX C. LM231 DATA SHEET .....  | 51 |
|      | APPENDIX D. SLR CONVERTER ONE LINE DIAGRAM .....                          | 67 |
|      | LIST OF REFERENCES .....  | 69 |
|      | INITIAL DISTRIBUTION LIST .....   | 71 |

THIS PAGE INTENTIONALLY LEFT BLANK

## LIST OF FIGURES

|            |   |    |
|------------|---|----|
| Figure 1.  | Energy storage system ratings. From [2].  | 2  |
| Figure 2.  | Energy storage comparisons. From [2].   | 3  |
| Figure 3.  | Laboratory lead acid battery string topology.                                       | 4  |
| Figure 4.  | Energy densities of predominant industrial sources. From [2].                       | 5  |
| Figure 5.  | EMS circuit schematic.  | 7  |
| Figure 6.  | EMS functional block diagram.   | 7  |
| Figure 7.  | Photograph of the EMS electronics.  | 8  |
| Figure 8.  | Series-loaded resonant converter printed circuit board.                             | 9  |
| Figure 9.  | Sensor circuitry.   | 10 |
| Figure 10. | Industry available battery balancing solutions. From [6].                           | 12 |
| Figure 11. | Standalone voltage-to-frequency converter. From [7].                                | 16 |
| Figure 12. | Simplified block diagram of standalone voltage to frequency converter.<br>From [7]. | 17 |
| Figure 13. | The laboratory setup.   | 18 |
| Figure 14. | Actual and theoretical battery bus voltage sensor 1 data comparison.                | 21 |
| Figure 15. | Actual and theoretical battery bus voltage sensor 2 data comparison.                | 22 |
| Figure 16. | Actual and theoretical temperature sensor 1 data comparison.                        | 24 |
| Figure 17. | Actual and theoretical temperature sensor 2 data comparison.                        | 25 |
| Figure 18. | Signal flowchart.   | 26 |
| Figure 19. | Edge detector and memory logic.   | 27 |
| Figure 20. | Signal biasing and filtering logic.   | 28 |
| Figure 21. | First order IIR low pass filter.  | 30 |
| Figure 22. | Multicell battery stack setup. From [11].   | 35 |
| Figure 23. | Battery balancing control logic.  | 37 |
| Figure 24. | Battery cell balancing control circuit.   | 38 |
| Figure 25. | Simulated individual battery cell voltage and associated control signal.            | 39 |
| Figure 26. | Individual cell voltage and SLR charger control ON signal.                          | 40 |
| Figure 27. | Individual cell voltage and SLR charger control OFF signal.                         | 41 |

THIS PAGE INTENTIONALLY LEFT BLANK

## LIST OF TABLES

|          |                              |    |
|----------|------------------------------|----|
| Table 1. | Voltage sensor 1.....        | 20 |
| Table 2. | Voltage sensor 2.....        | 21 |
| Table 3. | Temperature sensor 1.....    | 23 |
| Table 4. | Temperature sensor 2.....    | 24 |
| Table 5. | Sensor calibration data..... | 25 |

THIS PAGE INTENTIONALLY LEFT BLANK

## LIST OF ACRONYMS AND ABBREVIATIONS

|          |  |
|----------|--|
| TOC      | total ownership cost                           |
| DON      | Department of the Navy                         |
| TCA      | task critical assets                           |
| Li-ion   | lithium ion                                    |
| TOU      | time of use                                    |
| PCB      | printed circuit board                          |
| SLR      | series loaded resonant                         |
| FPGA     | field programmable gate array                  |
| V-to-F   | voltage-to-frequency                           |
| LM231    | precision voltage-to-frequency converter       |
| $V_s$    | LM231 input voltage                            |
| $V_{in}$ | LM231 maximum input signal swing               |
| $V_x$    | LM231 pin 6 voltage                            |
| $C_L$    | LM231 load capacitor                           |
| $R_L$    | LM231 load resistor                            |
| DC       | direct current                                 |
| $R_s$    | LM231 pin 2 reference voltage                  |
| $C_t$    | LM231 capacitance connected at pin 5           |
| $R_t$    | LM231 resistance connected from pin 5 to pin 8 |
| Ah       | amp-hour                                       |
| EMS      | energy management system                       |
| ROM      | read only memory                               |
| LUT      | lookup table                                   |
| $R^2$    | square of the correlation coefficient          |
| $R$      | correlation coefficient                        |
| IIR      | infinite impulse response                      |
| VHSIC    | very high speed integrated circuit             |
| VHDL     | VHSIC hardware description language            |
| LED      | light emitting diode                           |

THIS PAGE INTENTIONALLY LEFT BLANK

## **EXECUTIVE SUMMARY**

The Navy's dependence on reliable and redundant energy sources is staggering. In the past, the acquisition of Navy systems was approached from a performance centric viewpoint. Unfortunately, the decisions made in the acquisition process have long-lasting effects on the operation of shore and afloat assets. When energy efficiency is not a priority in the system design, the end result is a platform that may meet the performance needs of the Navy but will not meet the operations cost thresholds desired. Today, the Navy has shifted its acquisition plan to a focus on total ownership cost (TOC). Since the majority of the cost of a Navy system is incurred during its operational lifetime, instead of measuring the cost of system procurement, the Navy has started to estimate the cost to own and operate a system.

One of the primary operations costs incurred by Navy assets is energy consumption. In addition to the new focus on TOC, finding energy efficiencies and cost reductions has been identified as a strategic imperative by the Department of the Navy (DON). In [1], the Navy's shore facilities are tasked to, "ensure energy security as a strategic imperative ... achieve legal compliance for shore energy and sustainability ... and achieve Department of the Navy (DON) shore energy goals." Prior to this instruction and the broader focus on energy alternatives for Navy applications, there was no overarching strategy for achieving energy independence.

Of the tasks outlined in [1], the strategic imperative of energy security is directly related to the area of research covered in this thesis. The strategic imperative of energy security states that, "energy security is a critical component of national security. Energy security is having assured access to reliable supplies of energy and the ability to protect and deliver sufficient energy to meet operational needs afloat and ashore. Shore energy security for Navy is the mitigation of vulnerabilities related to the electrical grid, including outages from natural disaster, accident and physical and cyber attack." This section goes on to state that the Navy shall, "Provide reliable, resilient, and redundant mission critical energy sources to Navy tier I and II task critical assets (TCA) ashore," and "reduce vulnerabilities tied to the electrical grid, including outages from natural

disaster, accident, and physical and cyber attack, by lowering energy dependence and integrating energy security technologies which enable greater control of energy supply and distribution” [1]. One of the primary ways of bolstering our energy redundancy and thus decreasing our fossil fuel dependence is through the implementation of alternative energy sources. Although alternative energy solutions can be directly connected to the grid to support municipal and industrial loads, they can be optimized through their integration with energy storage and conversion systems.

There are numerous industry-available energy-storage systems on the market. They include hydrodynamics or pumped storage, numerous battery types, flywheels, double layer capacitors, and compressed air. The power ratings of the leading energy storage types with their associated discharge times are compared in Figure 1.

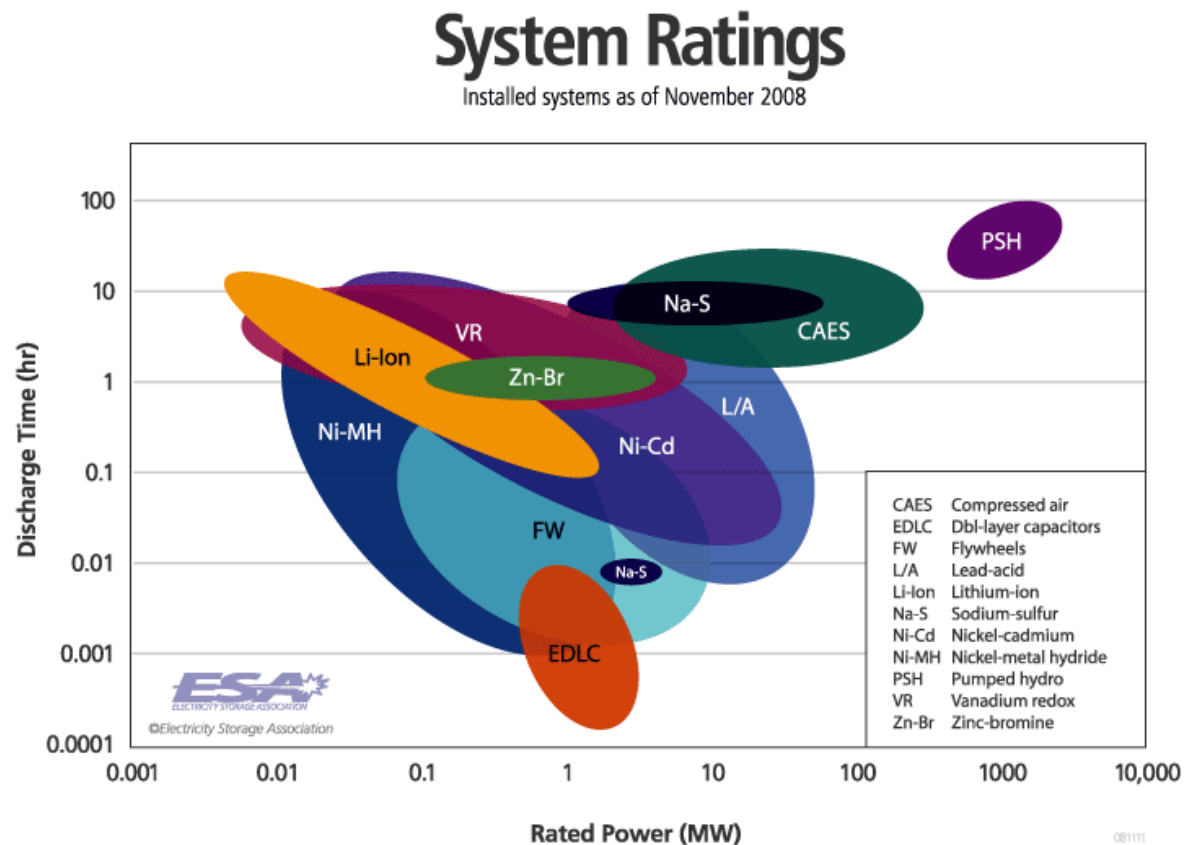


Figure 1. Energy storage system ratings. From [2].

In addition to the system design requirements that must be considered when choosing a storage type, other advantages and disadvantages must be thought through before committing to an energy storage type. The advantages, disadvantages, power, and energy applications of the energy storage types depicted in Figure 1 are listed in Figure 2.

| <b>Storage Technologies</b>           | <b>Main Advantages (relative)</b>                   | <b>Disadvantages (Relative)</b>                         | <b>Power Application</b> | <b>Energy Application</b> |
|---------------------------------------|---|---|--------------------------|---------------------------|
| Pumped Storage                        | High Capacity, Low Cost                             | Special Site Requirement                                |                          | ●                         |
| CAES                                  | High Capacity, Low Cost                             | Special Site Requirement, Need Gas Fuel                 |                          | ●                         |
| Flow Batteries:<br>PSB<br>VRB<br>ZnBr | High Capacity, Independent Power and Energy Ratings | Low Energy Density                                      | ○                        | ●                         |
| Metal-Air                             | Very High Energy Density                            | Electric Charging is Difficult                          |                          | ●                         |
| NaS                                   | High Power & Energy Densities, High Efficiency      | Production Cost, Safety Concerns (addressed in design)  | ●                        | ●                         |
| Li-ion                                | High Power & Energy Densities, High Efficiency      | High Production Cost, Requires Special Charging Circuit | ●                        | ○                         |
| Ni-Cd                                 | High Power & Energy Densities, Efficiency           |   | ●                        | ○                         |
| Other Advanced Batteries              | High Power & Energy Densities, High Efficiency      | High Production Cost                                    | ●                        | ○                         |
| Lead-Acid                             | Low Capital Cost                                    | Limited Cycle Life when Deeply Discharged               | ●                        | ○                         |
| Flywheels                             | High Power  | Low Energy density                                      | ●                        | ○                         |
| SMES, DSMES                           | High Power  | Low Energy Density, High Production Cost                | ●                        |                           |
| E.C. Capacitors                       | Long Cycle Life, High Efficiency                    | Low Energy Density                                      | ●                        | ○                         |

Fully capable and reasonable  
 Reasonable for this application  
 Feasible but not quite practical or economical  
 None  
 Not feasible or economical

Figure 2. Energy storage comparisons. From [2].

Lithium ion (Li-ion) batteries are one of the most promising energy storage solutions and the focus of this research. As can be seen in Figure 2, Li-ion batteries have power storage ratings that are fully capable of meeting consumer needs. Although the energy storage and control method is feasible, it still requires development and testing. Unfortunately, there are some risks associated with using lithium ion battery strings. A battery cell is a direct current device with a finite voltage rating based on cell type and design. Battery cells can be arranged in two configurations, depending on application. They can be connected in parallel, which results in a battery bank output voltage equal to an individual cell voltage. The other option is a series-connected string where each successive positive terminal is connected to the negative terminal of the next cell in the string. When battery cells are connected in series, their voltages are additive, thus, the total potential of the string can be boosted to voltage levels useful for energy storage and conversion. The battery string topology used in the laboratory at the Naval Postgraduate School is depicted in Figure 3.

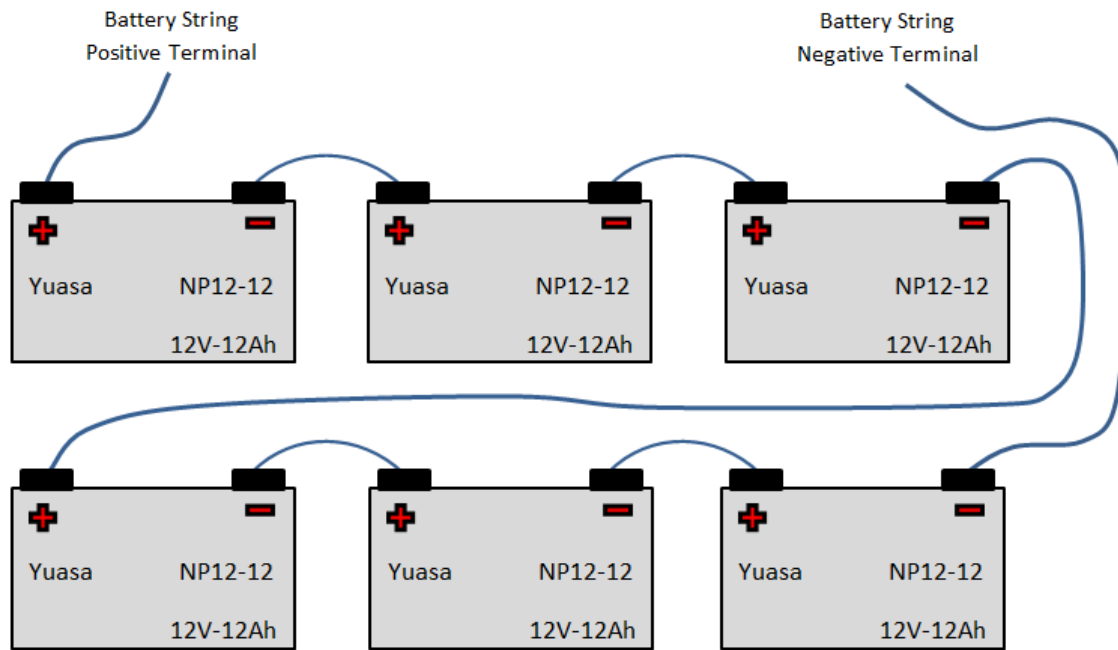


Figure 3. Laboratory lead acid battery string topology.

The lead acid battery cells purchased for use in the lab were specifically chosen to minimize the consequences if an over-charge condition occurs. When the limits of a lead acid cell are exceeded, the cell produces hydrogen gas as a byproduct. When a lithium ion battery experiences an overcharge condition, heat and possible fire are the result. In a well-ventilated area, hydrogen gas is a much more favorable consequence.

All battery strings are susceptible to individual cell temperature and voltage fluctuations. Due to variances in the manufacturing process, no two battery cells are identical. This inevitably results in a weak cell in a series connected string. As the battery string ages, the weakest cell in the string will have the largest voltage drop during discharge. These variances continue to grow overtime and can cause fire or explosion if parameters are left unchecked.

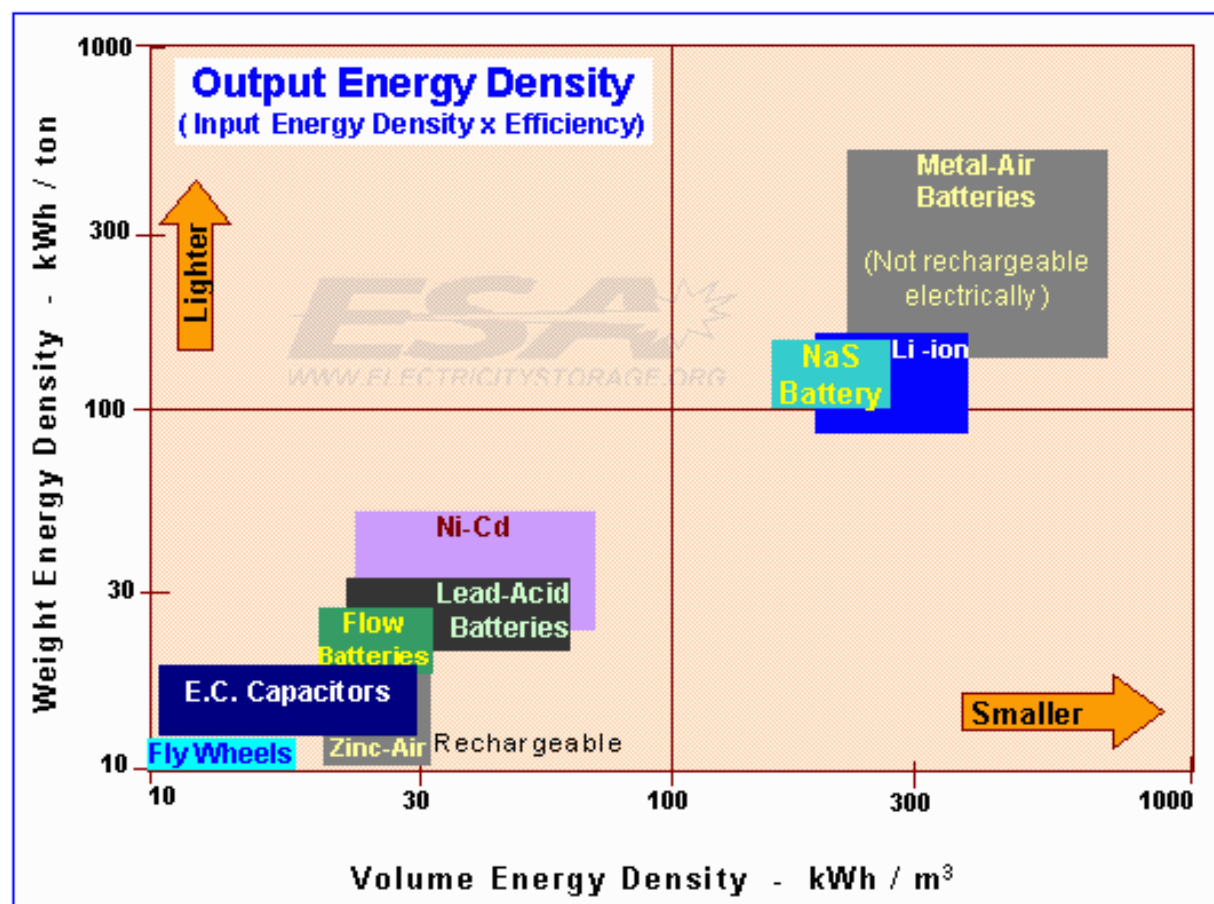


Figure 4. Energy densities of predominant industrial sources. From [2].

The comparative energy densities of the leading industrial power storage solutions are shown in Figure 4. Since lithium ion batteries have the highest energy density of all the rechargeable battery solutions, they are the obvious choice for maximum power storage and delivery [2]. The use of a lithium ion battery string is the most prudent approach to maximizing power storage for the consumer and the Navy, but it also possesses the most extreme consequences in a fault condition.

As industry has pursued the Li-ion energy storage there have been multiple casualties associated with Li-ion batteries. A fire occurred on the Advanced Seal Delivery System that was attributed to failure of a Li-ion cell. Additionally, a fire occurred in an emergency transmitter powered by a Li-ion battery string on a Boeing 787. These incidents highlight why accurately monitoring and controlling the state of charge during charge and discharge cycles is of utmost importance for lithium ion applications.

Energy conversion is the enabling technology for renewable energy sources such as wind turbines and photovoltaic arrays. Without safe and reliable energy storage, the power produced by these sources can be unreliable due to the intermittent nature of most renewable energy sources. As the limits of the power grid are continually extended, the demand for alternate power sources and smart appliances for residential use will continue to grow. The enabling technology for small consumer-based systems is microelectronics based power conversion and storage. There are many design topologies that can serve the power conversion and storage goal. A power electronics based energy management system (EMS) has recently been developed at Naval Postgraduate School to support the U.S. Navy needs to reduce energy consumption and enhance energy security [3], [4].

The goal of this research was to build and integrate series-loaded resonant (SLR) converters for use in balancing a series connected battery bank that is part of a broader system used for power storage and conversion. Voltage and temperature sensors are used to monitor individual cell state-of-charge and rate-of-charge and discharge. Voltage to frequency conversion is used to read sensor parameters. A battery balancing algorithm was designed, integrated and demonstrated with experimental results.

## LIST OF REFERENCES

- [1] Office of Naval Research. (2012, Jun. 22). *Shore energy management*. [Online]. Available: <http://greenfleet.dodlive.mil/files/2012/07/OPNAVINST-4100.5E.pdf>
- [2] Electricity Storage Association. *Technology comparisons*. [Online]. Available: [http://www.electricitystorage.org/technology/tech\\_archive/technology\\_comparisons](http://www.electricitystorage.org/technology/tech_archive/technology_comparisons)
- [3] G. Oriti, A. L. Julian, and N. J. Peck, “Power electronics enabled energy management systems,” in *Proc. of IEEE Appl. Power Electron. Conference (APEC)*, Long Beach, CA, Mar. 2013, pp. 3224–3231.
- [4] R. L. Kelly, A. L. Julian, and G. Oriti, “Reducing fuel consumption in a forward operating base using an energy management System,” in *Proc. of the IEEE 5th Energy Conversion Conference and Expo (ECCE)*, Denver, CO, Sept. 2013, pp. 1330–1336.

THIS PAGE INTENTIONALLY LEFT BLANK

## **ACKNOWLEDGMENTS**

I would like to thank my family members for their constant love and support. I would also like to thank Professor Alexander L. Julian for his patience throughout the research process. He has taught me that, with microelectronics, if you can dream it, you can build it.

THIS PAGE INTENTIONALLY LEFT BLANK

## I. INTRODUCTION

### A. BACKGROUND

The Navy's dependence on reliable and redundant energy sources is staggering. In the past, the acquisition of Navy systems was approached with a performance centric viewpoint. Unfortunately, the decisions made in the acquisition process have long-lasting effects on the operation of shore and afloat assets. When energy efficiency is not a priority in the system design, the end result is a platform that may meet the performance needs of the Navy but will not meet the operations cost thresholds desired. Today, the Navy has shifted its acquisition plan to a focus on total ownership cost (TOC). Because the majority of the cost of a Navy system is incurred during its operational lifetime, instead of measuring the cost of system procurement, the Navy has started to estimate the cost to own and operate a system.

One of the primary operational costs incurred by Navy assets is energy consumption. In addition to the new focus on TOC, finding energy efficiencies and cost reductions has been identified as a strategic imperative by the Navy. In [1], the Navy's shore facilities are tasked to, "ensure energy security as a strategic imperative...achieve legal compliance for shore energy and sustainability... and achieve Department of the Navy (DON) shore energy goals." Prior to this instruction and the broader focus on energy alternatives for Navy applications, there was no overarching strategy for achieving energy independence.

Of the tasks outlined in [1], the strategic imperative of energy security is directly related to the area of research covered in this thesis. The strategic imperative of energy security states that, "energy security is a critical component of national security. Energy security is having assured access to reliable supplies of energy and the ability to protect and deliver sufficient energy to meet operational needs afloat and ashore. Shore energy security for Navy is the mitigation of vulnerabilities related to the electrical grid, including outages from natural disaster, accident and physical and cyber attack." This section goes on to state that the Navy shall, "Provide reliable, resilient, and redundant

mission critical energy sources to Navy tier I and II task critical assets (TCA) ashore,” and “reduce vulnerabilities tied to the electrical grid, including outages from natural disaster, accident, and physical and cyber attack, by lowering energy dependence and integrating energy security technologies which enable greater control of energy supply and distribution” [1]. One of the primary ways of bolstering our energy redundancy and, thus, decreasing our fossil fuel dependence is through the implementation of alternative energy sources. Although alternative energy solutions can be directly connected to the grid to support municipal and industrial loads, they can be optimized through their integration with energy storage and conversion systems.

## B. ENERGY STORAGE

There are numerous industry available energy storage systems on the market. They include hydrodynamics or pumped storage, numerous battery types, flywheels, double layer capacitors, and compressed air. The power ratings of the leading energy storage types with their associated discharge times are compared in Figure 1.

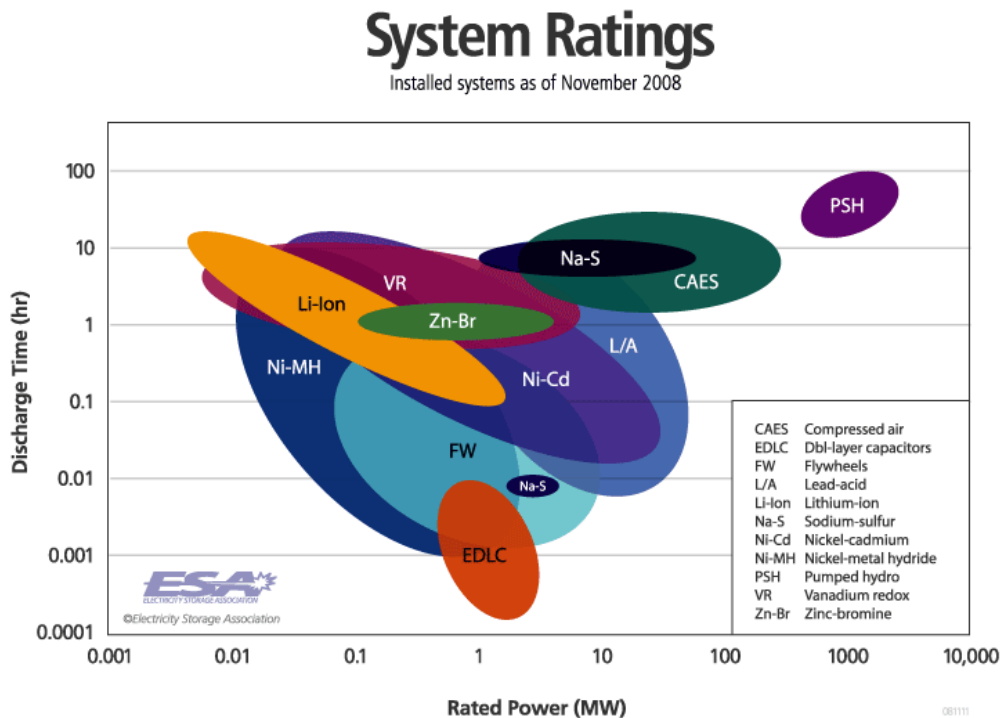


Figure 1. Energy storage system ratings. From [2].

In addition to the system design requirements that must be considered when choosing a storage type, other advantages and disadvantages must be thought through before committing to an energy storage type. The advantages, disadvantages, power, and energy applications of the energy storage types depicted in Figure 1 are listed in Figure 2.

| <b>Storage Technologies</b>           | <b>Main Advantages (relative)</b>                   | <b>Disadvantages (Relative)</b>                         | <b>Power Application</b> | <b>Energy Application</b> |
|---------------------------------------|---|---|--------------------------|---------------------------|
| Pumped Storage                        | High Capacity, Low Cost                             | Special Site Requirement                                |                          | ●                         |
| CAES                                  | High Capacity, Low Cost                             | Special Site Requirement, Need Gas Fuel                 |                          | ●                         |
| Flow Batteries:<br>PSB<br>VRB<br>ZnBr | High Capacity, Independent Power and Energy Ratings | Low Energy Density                                      | ○                        | ●                         |
| Metal-Air                             | Very High Energy Density                            | Electric Charging is Difficult                          |                          | ●                         |
| NaS                                   | High Power & Energy Densities, High Efficiency      | Production Cost, Safety Concerns (addressed in design)  | ●                        | ●                         |
| Li-ion                                | High Power & Energy Densities, High Efficiency      | High Production Cost, Requires Special Charging Circuit | ●                        | ○                         |
| Ni-Cd                                 | High Power & Energy Densities, Efficiency           |   | ●                        | ○                         |
| Other Advanced Batteries              | High Power & Energy Densities, High Efficiency      | High Production Cost                                    | ●                        | ○                         |
| Lead-Acid                             | Low Capital Cost                                    | Limited Cycle Life when Deeply Discharged               | ●                        | ○                         |
| Flywheels                             | High Power  | Low Energy density                                      | ●                        | ○                         |
| SMES, DSMES                           | High Power  | Low Energy Density, High Production Cost                | ●                        |                           |
| E.C. Capacitors                       | Long Cycle Life, High Efficiency                    | Low Energy Density                                      | ●                        | ○                         |

Fully capable and reasonable  
 Reasonable for this application  
 Feasible but not quite practical or economical  
 None  
 Not feasible or economical

Figure 2. Energy storage comparisons. From [2].

Lithium ion (Li-ion) batteries are one of the most promising energy storage solutions and the focus of this research. As can be seen in Figure 2, Li-ion batteries have power storage ability that is fully capable of meeting consumer needs. Although the energy storage and control method is feasible, it still requires development and testing. Unfortunately, there are some risks associated with using lithium ion battery strings. A battery cell is a direct current device with a finite voltage rating based on cell type and design. Battery cells can be arranged in two configurations depending on application. They can be connected in parallel, which results in a battery bank output voltage equal to an individual cell voltage. The other option is a series connected string where each successive positive terminal is connected to the negative terminal of the next cell in the string. When battery cells are connected in series, their voltages are additive, thus, the total potential of the string can be boosted to voltage levels useful for energy storage and conversion. The battery string topology used in the laboratory is depicted in Figure 3.

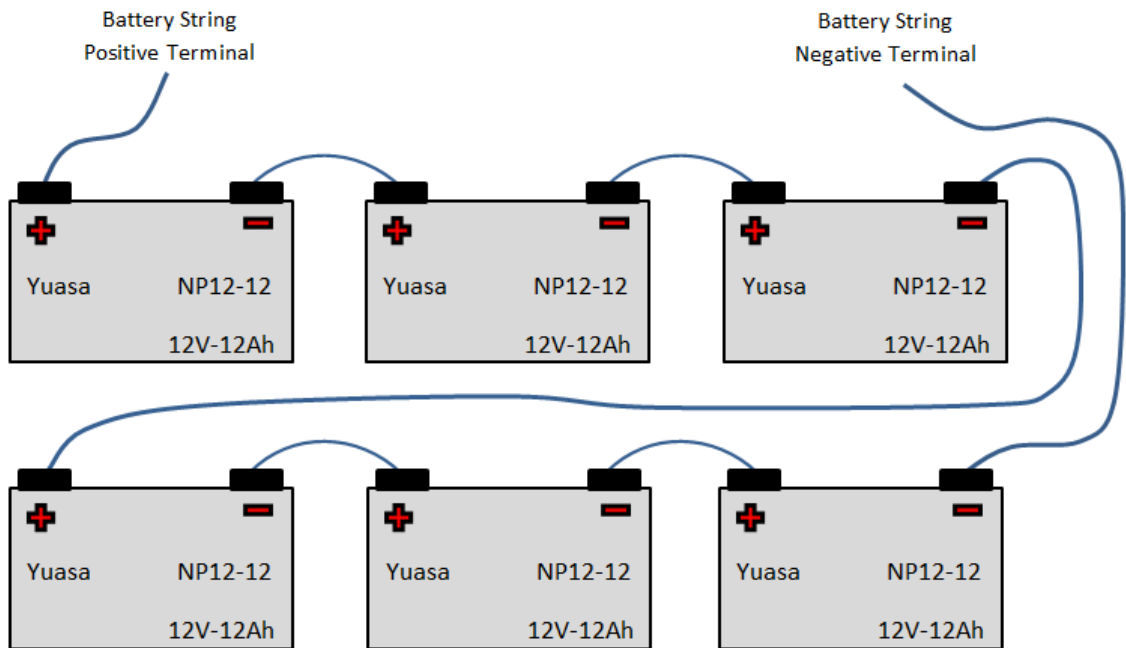


Figure 3. Laboratory lead acid battery string topology.

The lead acid battery cells purchased for use in the lab were specifically chosen to minimize the consequences if an over-charge condition occurs. When the limits of a lead acid cell are exceeded, the cell produces hydrogen gas as a byproduct. When a lithium ion battery experiences an overcharge condition, heat and possible fire are the result. In a well-ventilated area, hydrogen gas is a much more favorable consequence.

All battery strings are susceptible to individual cell temperature and voltage fluctuations. Due to variances in the manufacturing process, no two battery cells are identical. This inevitably results in a weak cell in a series connected string. As the battery string ages, the weakest cell in the string will have the largest voltage drop during discharge. These variances continue to grow over time and can cause fire or explosion if parameters are left unchecked.

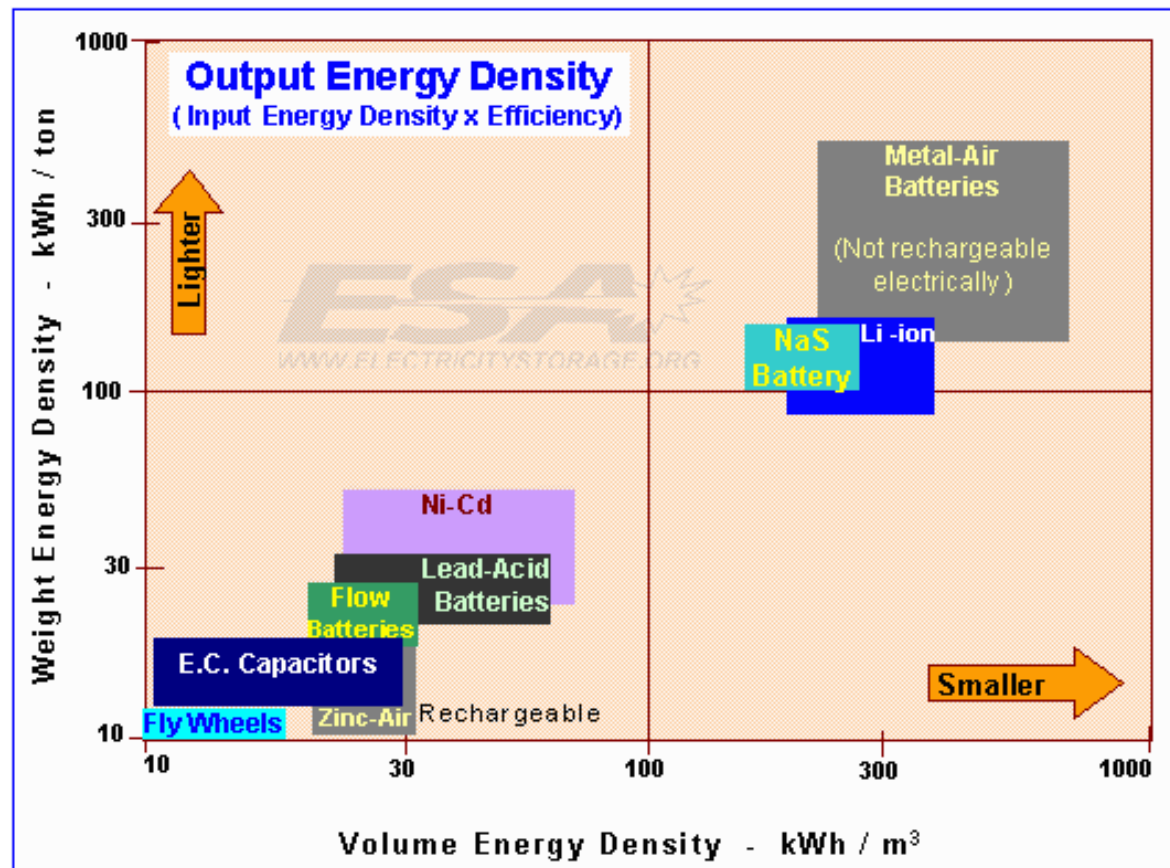


Figure 4. Energy densities of predominant industrial sources. From [2].

The comparative energy densities of the leading industrial power storage solutions are shown in Figure 4. Since lithium ion batteries have the highest energy density of all the rechargeable battery solutions, they are the obvious choice for maximum power storage and delivery [2]. The use of a lithium ion battery string is the most prudent approach to maximizing power storage for the consumer and the Navy, but it also possesses the most extreme consequences in a fault condition. As industry has pursued the Li-ion technology there have been multiple casualties associated with Li-ion batteries. A fire occurred on the Advanced Seal Delivery System that was attributed to failure of a Li-ion cell. Additionally, a fire occurred in an emergency transmitter powered by a Li-ion battery string on a Boeing 787. These incidents highlight why accurately monitoring and controlling the state of charge during charge and discharge cycles is of utmost importance for lithium ion applications.

### C. ENERGY CONVERSION

Energy conversion is the enabling technology for renewable energy sources such as wind turbines and photovoltaic arrays. Without safe and reliable energy storage, the power produced by these sources can be unreliable due to the intermittent nature of most renewable energy sources. As the limits of the power grid are continually extended, the demand for alternate power sources and smart appliances for residential use will continue to grow. The enabling technology for small consumer based systems is microelectronics based power conversion and storage. There are many design topologies that can serve the power conversion and storage goal. A power electronics based energy management system (EMS) has recently been developed at Naval Postgraduate School (NPS) to support the Navy's goal to reduce energy consumption and enhance energy security [3], [4].

The EMS consists of a local series-connected battery bank interfaced to the power grid via a field programmable gate array (FPGA) controlled power converter. The EMS circuit schematic is shown in Figure 5, with the associated functional block diagram in Figure 6 and a picture of the EMS printed circuit board is included as Figure 7.

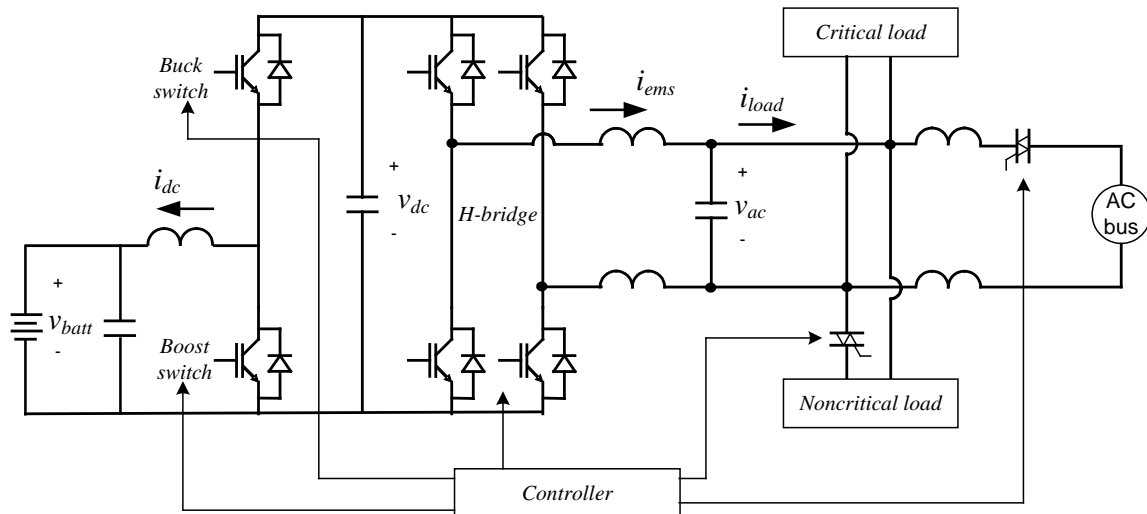


Figure 5. EMS circuit schematic.

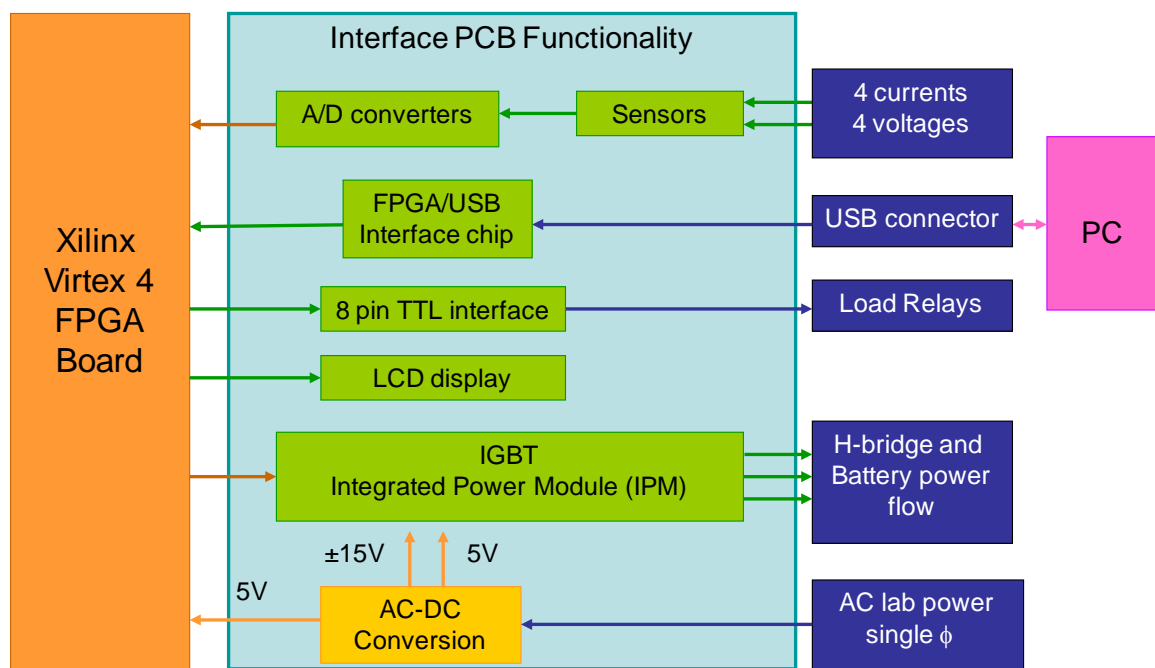


Figure 6. EMS functional block diagram.

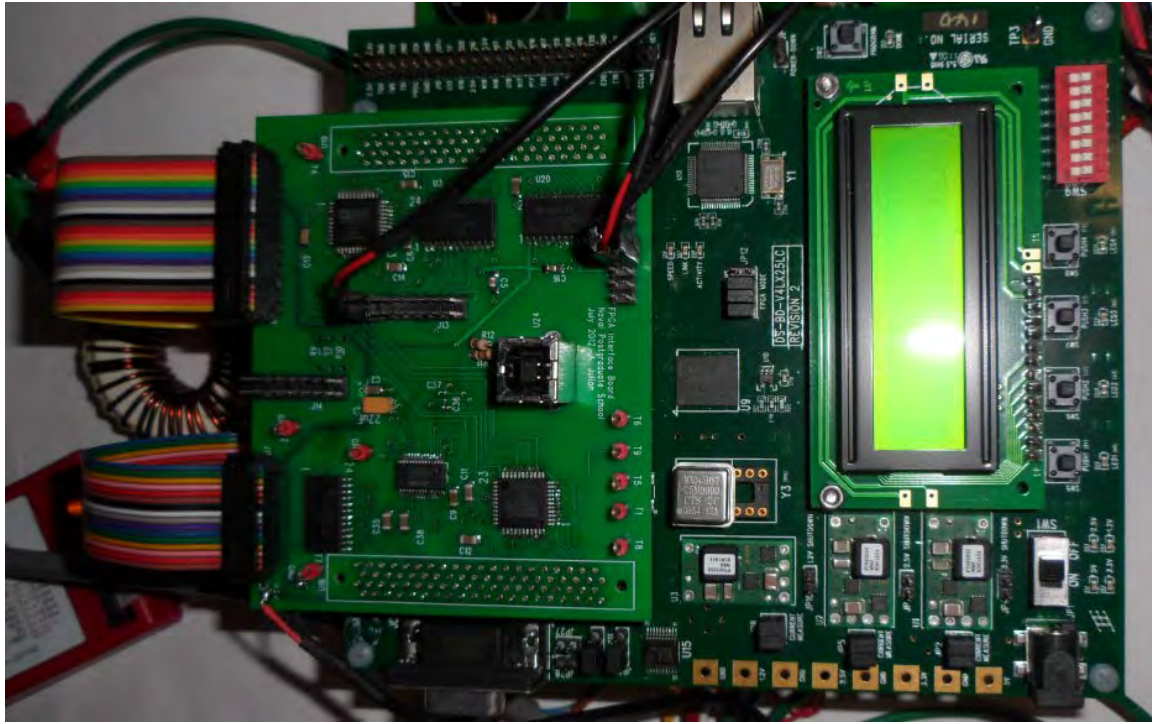


Figure 7. Photograph of the EMS electronics.

The EMS has many capabilities, including the ability to store power during off peak hours when electricity is cheap and return that power during high peak hours or in the event of power interruption. This technique achieves electricity cost reduction for users, such as large Navy facilities, where there is a time of use (TOU) contract with the power company. In this contract type, the Navy pays different rates for power delivered at different times of the day. The EMS provides redundancy and flexibility while interfacing with renewable energy sources, which allows the user to leverage green technology solutions such as solar and wind power. As an example, a solar panel can be used to recharge the batteries instead of energy drawn from the main grid.

The goal of this research is to build and integrate series-loaded resonant (SLR) converters for use in balancing a series-connected battery bank that is part of a broader system used for power storage and conversion. Included at the end of this thesis is a set of appendices which are intended to provide easy access to relevant technical information directly related to this research area. The first appendix, Appendix A, is the battery balancing algorithm developed to control the individual state-of-charge of each battery

cell in the laboratory battery string. The second appendix, Appendix B, is the initial conditions file that establishes a set of variables at startup to allow the MATLAB program to run. The third appendix, Appendix C, is a copy of the data sheet for the precision voltage-to-frequency converter chip that is a major focus of this research. The physical layout of the SLR converter used in this research is shown in Figure 8. A wiring diagram of the PCB shown in Figure 7 is included as Appendix A. Additionally, the temperature and voltage sensing circuits are also integrated on the board shown in Figure 8 since each battery cell has its own independent calibrated sensors.

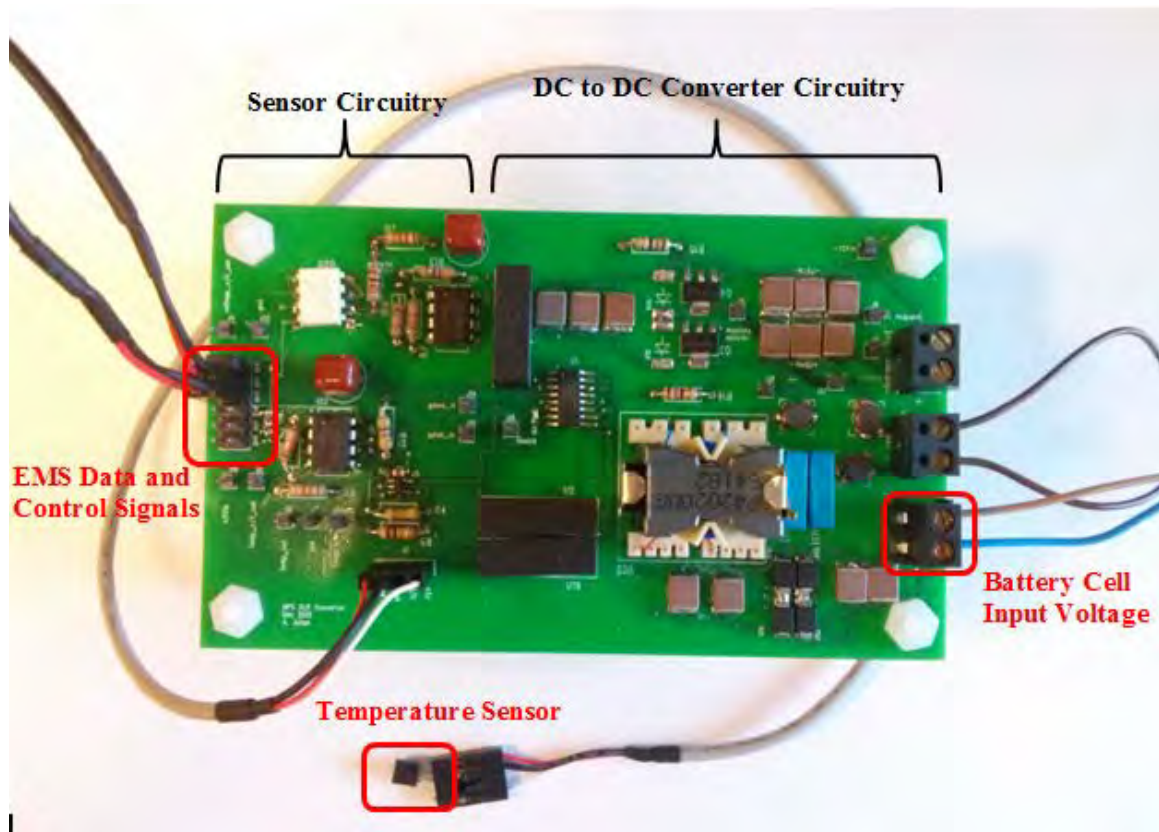


Figure 8. Series-loaded resonant converter printed circuit board.

Voltage and temperature sensors are used to monitor individual cell state-of-charge and rate-of-charge and discharge. The sensor circuitry is shown in Figure 8 to illustrate its board location relative to the power conversion circuitry, the converter input and output pins and the temperature sensor used. Figure 9 is a close-up picture of the

sensor circuitry to highlight the types of chips used and their respective physical locations on the board.

The goal of this research is to build and integrate a bank of series-loaded resonant (SLR) converters for use in balancing a series-connected battery bank that is part of a broader system used for power storage and conversion.

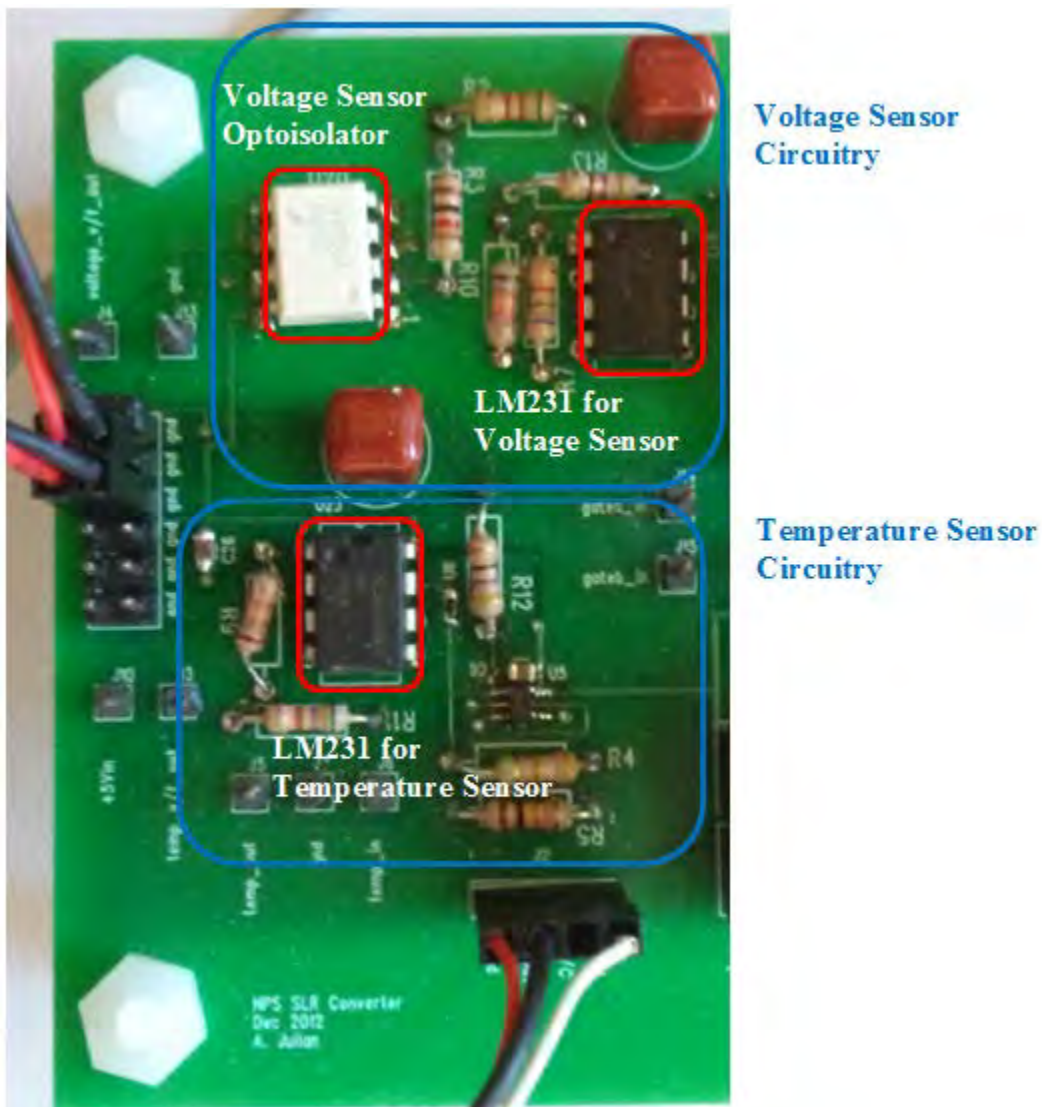


Figure 9. Sensor circuitry.

The voltage and temperature sensors depicted above can be used to monitor individual cell state-of-charge and rate-of-charge and discharge. Voltage-to-frequency

conversion is used to read sensor parameters. A battery balancing algorithm is designed, integrated and demonstrated with experimental results.

#### **D. BATTERY BALANCING**

To safely operate a series-connected battery string, individual cell balancing must be employed. Variation in manufacturing processes causes deviations from design tolerances, which causes each battery cell in a string to have a different expected lifetime. Today, many topologies use series-connected battery cells, and the battery string is only as good as the cell with the weakest expected lifetime. Sadly, when a cell nears the end of its useful life, the whole string must be replaced. If the old cell was replaced with a new cell, the problem of string imbalance would be perpetuated, since the capacity of the new cell would be much greater than the other cells in the aging string [5].

The consequences of cell imbalance can be quite catastrophic. Without individual cell monitoring, malfunctions can go unnoticed. If a cell is malfunctioning, the failure can manifest itself as a difference in voltage or higher temperature. Charging past this point to bring the whole string to the normal operating voltage will cause the temperature of the weak cell to increase and the voltage to decrease. The results of such a failure depend on the type of batteries in the string and the size of the individual cells [5].

If a battery string utilizes large cells, the internal energy of any one cell is large as well. If overcharging of an aging cell occurs, the internal energy of the cell can be released very quickly. For lead acid batteries, overcharging causes hydrogen gas production, which is flammable or explosive. Although hydrogen gas production is not a desired result of charging, compared to the consequences of an overcharge condition with nickel cadmium or lithium ion batteries, hydrogen gassing is preferred. For a similar set of fault conditions, a Lithium Ion battery has a much higher likelihood of causing fire or explosion. When large battery cells are used and a fault is present, the resultant individual cell fire or explosion can cause a ripple effect through the string resulting in release of all the internal energy of the battery string, an obvious safety hazard and liability [5].

Many modern-day battery topologies use much smaller cells in the string to prevent the catastrophic ripple effects of individual cell failure. The benefits are obvious;

if the cell is sized correctly, the failure can be localized. The drawback is a complex battery string topology and associated control architecture. The increases in complexity lead to higher design and manufacturing costs. There is a prevalence of small inexpensive Lithium Ion cells due to the consumer electronics industry, which in some applications may alleviate the higher cost of design and layout [5].

The battery imbalance problem has been known in industry for many years. Traditional battery balancing methods, often referred to as passive balancing, involve inefficient and antiquated solutions. The most popular old-world passive balancing method uses discharge resistors to prevent a cell from reaching a charge greater than its neighbors. Various industry available battery balancing design options are shown in Figure 10 to demonstrate the multitude of solutions available.

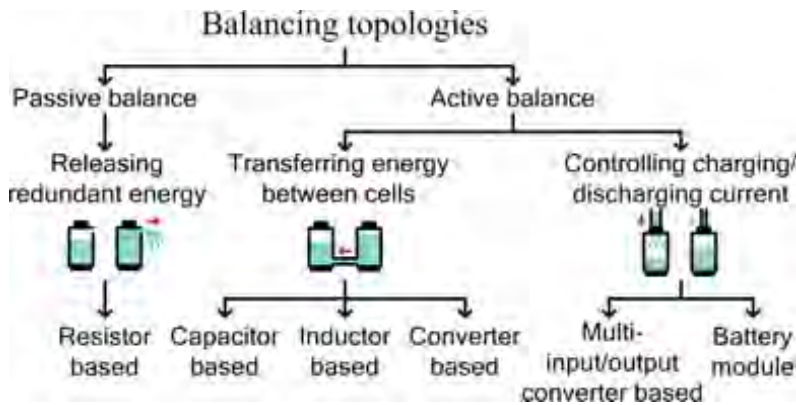


Figure 10. Industry available battery balancing solutions. From [6].

Another common solution involves limiting the battery charge to the maximum state of charge of the weakest cell. This, of course, requires battery-cell monitoring and prevents maximum utilization of the battery string's energy storage capabilities. In all cases, the employment of modern-day microelectronics can yield higher efficiencies during cell balance charge and discharge as well as greater utilization of the string and, thus, a longer lifespan [6].

The benefits of utilizing microelectronics in an active battery balancing system, with individual cell monitoring and control, are proliferous. The battery string can be safely operated with lithium ion battery cells, thereby maximizing the string energy

density. With safe monitoring and control, the operation of each cell can be monitored throughout life. The cells that show early signs of fatigue can be preferentially unloaded during high rates of charge and discharge, thereby extending their useful life and the life of the entire battery string.

The goal of this research is to develop a battery balancing algorithm for a series-connected battery string. To achieve this result, an individual cell voltage and temperature sensor must be designed, built and integrated into the EMS. Conversion of the analog temperature and voltage signals into digital signals for transmission is discussed in Chapter II. Additionally, the processing of the digital data within the FPGA of the EMS is covered in Chapter II. The development and integration of the battery balancing algorithm and associated results during implementation and testing is discussed in Chapter III. Conclusions and future work are covered in Chapter IV.

THIS PAGE INTENTIONALLY LEFT BLANK

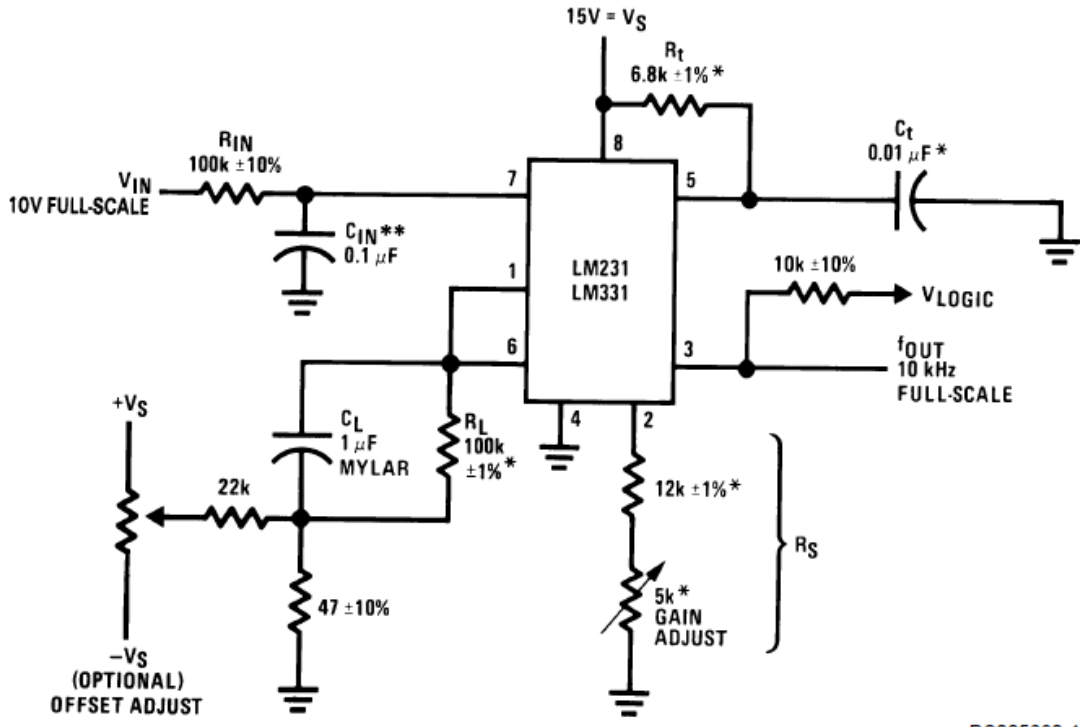
## **II. ANALOG-TO-DIGITAL CONVERSION AND PROCESSING**

Microelectronics are used to sense the voltage and the temperature of each battery cell in the string. A voltage-to-frequency (V-to-F) converter generates a digital waveform that is a square wave, where the frequency of the square wave is a function of the measured quantity. This square wave is reinterpreted in the FPGA to a digital quantity for the voltage or temperature being measured.

### **A. OPERATION OF THE PRECISION VOLTAGE-TO-FREQUENCY CONVERTER (LM231)**

Voltage-to-frequency control is one of the most prevalent methods of transmitting digital data over a long distance for measurement by a control system. The reason for its widespread use in industry is due to the benefits digital data provides through the analog-to-digital conversion process. Over long distances analog data on a line can be corrupted by numerous external factors which contribute to signal noise and attenuation. Given these advantages, the application of V-to-F control for the battery string sensors in the EMS system is prudent. The sensor circuitry on the SLR converters will likely be located some distance from the EMS to avoid cascading failures if there were an individual battery cell fault condition. Since the EMS end state architecture is not fully known now, providing the system with extra flexibility and a higher level of redundancy during the design and prototyping phases is good practice.

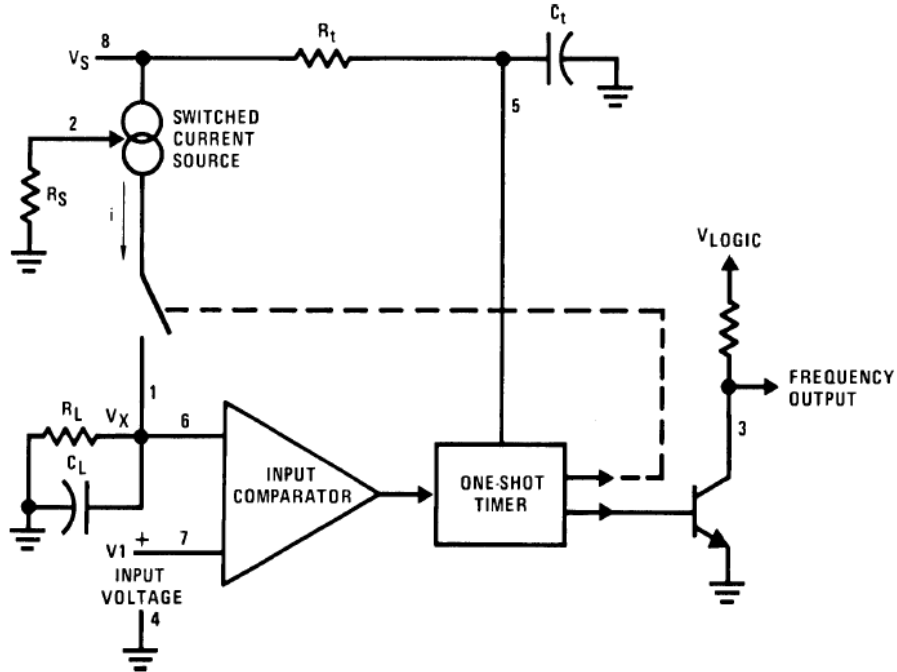
Conversion of an analog voltage input level to variable frequency pulses makes the data less susceptible to error, and V-to-F control is achieved. The system design requires a device that is insensitive to external factors and an output that varies linearly with input voltage. The precision voltage-to-frequency converter (LM231) is one such solution. The circuit topology used in the lab for V-to-F conversion is indicated in Figure 11.



DS005680-1

Figure 11. Standalone voltage-to-frequency converter. From [7].

As the voltage input to the chip is varied, the chip creates pulses whose period is linearly proportional to the voltage input signal. Although V-to-F control is simple and straightforward to use, there are some details that are important to emphasize. The design of the LM231 requires an input voltage  $V_s$  of 15 volts DC at pin 8, with an associated ground connection at pin 4. The maximum input signal swing  $V_{in}$  is then constrained to two thirds of  $V_s$ , or 10 volts DC at pin 7, as shown in Figure 11. These set points are vital to the proper operation of the chip, sensor and converter. If the ratio of  $V_s$  to  $V_{in}$  is out of specification, saturation within the chip can result and the useful range of voltage readings is limited. This may seem trivial; however, the sensor data will be used to control the on and off state of lithium ion batteries which have the potential for fire if individual cell failure occurs [5]. A functional representation of a V-to-F converter that correlates to the pins of Figure 11 is shown in Figure 12.



DS005680-4

Figure 12. Simplified block diagram of standalone voltage to frequency converter.  
From [7].

With power and input signal levels from the board set at design specifications for the chip, the internal operation of the LM231 can be discussed. The numbers in Figure 12 correspond to the pin out shown in Figure 11. When  $V_{in}$  is higher than the voltage at pin 6  $V_x$ , the input comparator triggers the one shot timer, which turns on the switched current source and biases the gate of the transistor at pin 3. With the transistor at pin 3 on, the output pin is pulled low. The output remains low for a fixed period of time  $t$ , where

$$t = 1.1R_tC_r. \quad (1)$$

The constant  $R_t$  is the resistance value between pin 5 and pin 8 shown in Figure 12. The constant  $C_t$  is the capacitance between pin 5 and ground shown in Figure 12. This constant low value is set during circuit design and thus, does not change throughout the calibration process. During the data collection process, we observed the constant low value on the oscilloscope as an unchanging low signal between the measured varying high values.

The voltages  $V_{in}$  and  $V_x$  rebalance through the charging of the load capacitor  $C_L$  via the switched current source. When the switch for the switched current source opens, the charge collected on  $C_L$  discharges to ground via the load resistor  $R_L$  until  $V_{in}$  is greater than  $V_x$  and the cycle repeats. It is important to note that the V-to-F cycle can be operated in reverse, where the input would be a digital signal with varying frequency and the output would be a linearly proportional analog voltage output [7].

## B. MEASURING THE SIGNAL OUTPUT

With the design parameters of the LM231 established and the circuit board designed and built, the actual output data can be measured and compared to the theoretical data. This serves two purposes. One, the actual data must be measured to verify proper operation of the LM231, confirming that the output signals are varying linearly. Two, the actual data values are used to determine the direct current (DC) offset of the signal and the proper biasing, which are used in the control logic discussed in Section C. The laboratory measurements were made on the test equipment as configured in Figure 13.

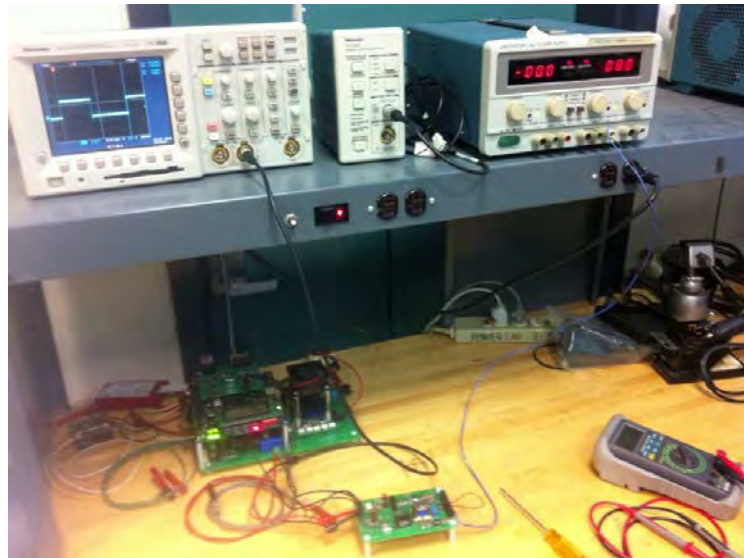


Figure 13. The laboratory setup.

The measurement setup employs another variable DC power source to simulate the battery bus voltage which is the input voltage in Figure 12. The expected operating point of each battery is twelve volts; therefore, data is taken at half volt increments from eight volts DC to fourteen volts DC. As the simulated battery bus voltage is increased, the oscilloscope is used to measure output frequency pulses. The period of a pulse at each battery voltage threshold is recorded and converted to an associated frequency value. While taking the data measurements, saturation is observed just above 13.5 V. If this occurred at a voltage closer to the battery string operating point, the circuit board design would have to be reevaluated and re-biased to ensure that the input signal swing avoided saturation conditions of the LM231.

After recording the actual data, the corresponding theoretical data is calculated for comparison. The theoretical output frequency of the circuit in Figure 11 is

$$f_{out} = \frac{V_{in}}{2.09} \frac{R_s}{R_L} \frac{1}{R_t C_t} \quad (2)$$

where  $V_{in}$  is the input voltage level, 2.09 is a conversion factor,  $R_s$  creates a reference voltage at pin 2 and is 10 kΩ, and  $R_L$ , set at 100 kΩ and connected to pin 6, affects the discharge rate of  $C_L$  shown in Figure 11. The capacitance  $C_t$  is connected to pin 5 and is 0.01 μF, and the associated resistance  $R_t$  is 6.8kΩ and is connected from pin 5 to pin 8. These values set the time response of the one-shot timer [7]. Actual and theoretical data defined by Equation (2) is plotted in Figure 14. The measured data is fitted with a linear trend line shown in Figure 14 and Figure 15, with associated the DC offset and V-to-F slope values shown in Table 5.

### C. CALIBRATION RESULTS

With the system's analog-to-digital sensors built and their operation verified, operating ranges are chosen and calibration data is taken. To measure the battery voltage, a direct current power converter is used to input variable voltage thresholds to the voltage measurement circuit. The battery cells used for the system are NP12–12, with a nominal voltage of 12 V and an amp-hour (Ah) rating of 12 Ah [8]. With an individual cell voltage of 12 V, a data range of 8 V to 14 V is chosen.

Initially, the signal frequency is read using the channel frequency output on the oscilloscope. Unfortunately, as the simulated battery bus voltage is increased, the channel frequency measurement made by the mathematical function of the oscilloscope starts to oscillate. The range of oscillation is so bad that another method had to be employed.

Although the channel frequency output is noisy, it is possible to measure the pulse frequency indirectly by using the cursors on the oscilloscope to measure the signal period. The battery voltage operating range is chosen to be symmetric around the battery operating point of 12 V, thus the range of measurement is from 8 V to 14 V. Saturation of the chip is observed just past 13.5 V, making the 14 V point immeasurable. The measured and associated theoretical voltage sensor data is shown in Table 1 and Table 2. The theoretical data is calculated in Excel using Equation (2) and represented with a red square. From the measured data in Table 1 and Table 2, graphs of the actual and theoretical data are overlaid and included as Figure 14 and Figure 15.

Table 1. Voltage sensor 1.

| Battery Voltage (V) | Measured Data     |                | Theoretical Data |
|---------------------|-------------------|----------------|------------------|
|                     | Period ( $\mu$ s) | Frequency (Hz) | Frequency (Hz)   |
| 8.000               | 137.000           | 7299.270       | 7880.664         |
| 8.500               | 130.000           | 7692.308       | 8373.206         |
| 9.000               | 123.000           | 8130.081       | 8865.747         |
| 9.500               | 116.000           | 8620.690       | 9358.289         |
| 10.000              | 111.000           | 9009.009       | 9850.830         |
| 10.500              | 105.000           | 9523.810       | 10343.372        |
| 11.000              | 100.000           | 10000.000      | 10835.913        |
| 11.500              | 96.000            | 10416.667      | 11328.455        |
| 12.000              | 91.600            | 10917.031      | 11820.996        |
| 12.500              | 88.400            | 11312.217      | 12313.538        |
| 13.000              | 85.200            | 11737.089      | 12806.079        |
| 13.500              | 82.000            | 12195.122      | 13298.621        |

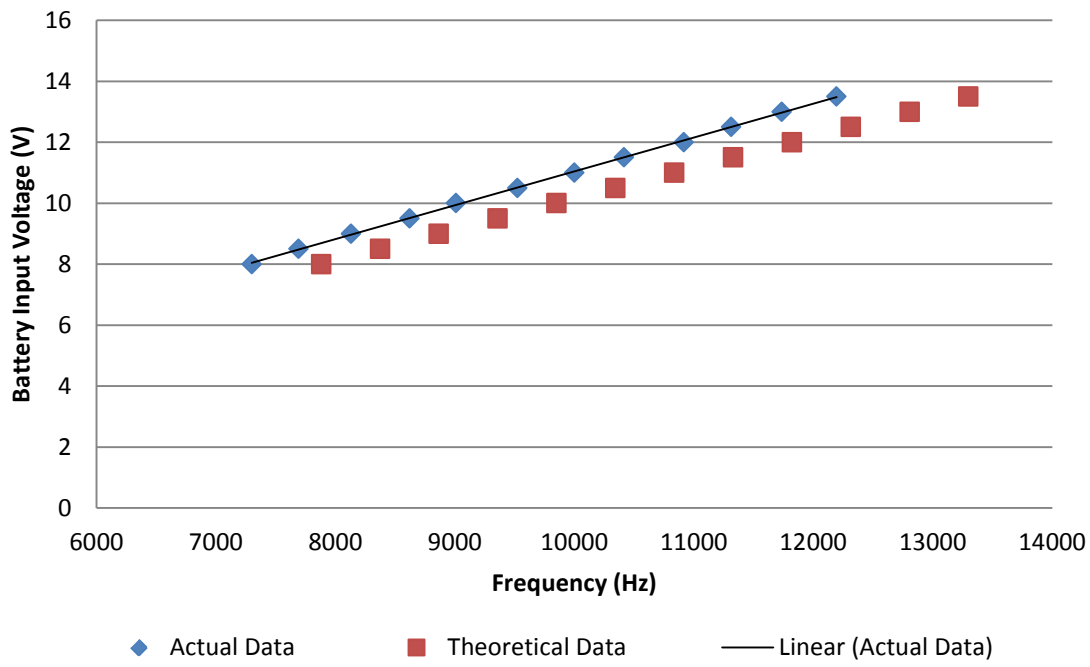


Figure 14. Actual and theoretical battery bus voltage sensor 1 data comparison.

Table 2. Voltage sensor 2

| Battery Voltage (V) | Measured Data     |                | Theoretical Data |
|---------------------|-------------------|----------------|------------------|
|                     | Period ( $\mu$ s) | Frequency (Hz) | Frequency (Hz)   |
| 8.000               | 135.000           | 7407.407       | 7880.664         |
| 8.500               | 127.000           | 7874.016       | 8373.206         |
| 9.000               | 120.000           | 8333.333       | 8865.747         |
| 9.500               | 114.000           | 8771.930       | 9358.289         |
| 10.000              | 108.000           | 9259.259       | 9850.830         |
| 10.500              | 103.000           | 9708.738       | 10343.372        |
| 11.000              | 98.000            | 10204.082      | 10835.913        |
| 11.500              | 94.000            | 10638.298      | 11328.455        |
| 12.000              | 90.400            | 11061.947      | 11820.996        |
| 12.500              | 86.800            | 11520.737      | 12313.538        |
| 13.000              | 83.200            | 12019.231      | 12806.079        |
| 13.500              | 78.400            | 12755.102      | 13298.621        |

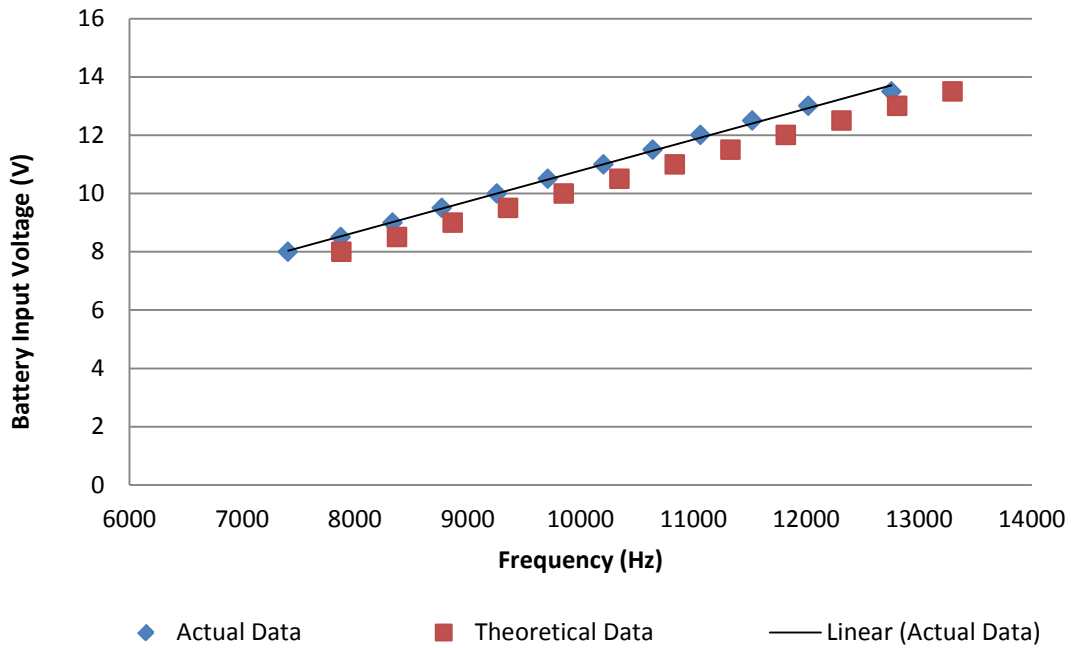


Figure 15. Actual and theoretical battery bus voltage sensor 2 data comparison.

After the data for the voltage sensors are recorded, the laboratory setup is modified to take data for the temperature sensor, which proved to be more complex than initially anticipated. The major problem encountered while taking temperature data is creating a stable temperature input. The first attempt involved wiring up a  $48\text{ k}\Omega$  resistor to an adjustable direct current power converter to generate heat. The temperature sensor was then taped to the resistor, and the input voltage to the resistor was varied to generate heat which was then transferred via conduction to the temperature sensor. In theory, as the voltage to the resistor is increased, the power consumed by the resistor linearly increases. The power consumed by the resistor is dissipated to ambient as heat. In practice the time response for heat generation is slow and inaccurate. As voltage is increased, the tape on the temperature sensor started to melt and the geometry between the resistor and temperature sensor changed which changed the data. It was quickly evident that using a resistor as a heat source caused too much variation in the system and did not generate a good data set.

After stepping back and thinking about the problem, it was evident that the previous idea is too complex. There are too many sources of variation. Next, a heat gun was acquired and the laboratory setup was adjusted so that the temperature sensor could be placed in the heat gun to generate different temperature levels, but again problems are encountered. The temperature sensor is so sensitive to the heat input that it is difficult to hold the temperature constant so that the output frequency pulses can be measured.

The solution presented itself when it was observed that, although the time response for heating the temperature sensor was fast, the time response for cooling was slow enough that there was time to observe the data. Additionally, instead of picking varying temperature thresholds and measuring the frequency data, the cursors on the oscilloscope were set to discrete levels and the temperature adjusted. Generating good data using this method required some practice. The best method involved setting a desired output signal period threshold. Then, by heating the temperature sensor past the output signal period, voltage input observations can be recorded as the sensor cools past the output signal period threshold. The measured and associated theoretical voltage sensor data is shown in Table 3 and Table 4. The theoretical data is calculated in Excel using Equation 2. From the measured data in Table 3 and Table 4, graphs of the actual and theoretical data are overlaid and included as Figure 16 and Figure 15.

Table 3. Temperature sensor 1.

|                                     |                                     | Measured Data |                | Theoretical Data |
|-------------------------------------|-------------------------------------|---------------|----------------|------------------|
| Temp Sensor Input Voltage (V) Run 1 | Temp Sensor Input Voltage (V) Run 2 | Period (μs)   | Frequency (Hz) | Frequency (Hz)   |
| 0.281                               | 0.282                               | 700           | 1428.571       | 1107.233         |
| 0.302                               | 0.300                               | 650           | 1538.462       | 1189.980         |
| 0.324                               | 0.327                               | 600           | 1666.667       | 1276.668         |
| 0.352                               | 0.352                               | 550           | 1818.182       | 1386.997         |
| 0.382                               | 0.392                               | 500           | 2000.000       | 1505.207         |
| 0.425                               | 0.423                               | 450           | 2222.222       | 1674.641         |
| 0.466                               | 0.475                               | 400           | 2500.000       | 1836.195         |
| 0.528                               | 0.544                               | 350           | 2857.143       | 2080.495         |
| 0.612                               | 0.594                               | 300           | 3333.333       | 2411.483         |
| 0.698                               | 0.689                               | 250           | 4000.000       | 2750.352         |

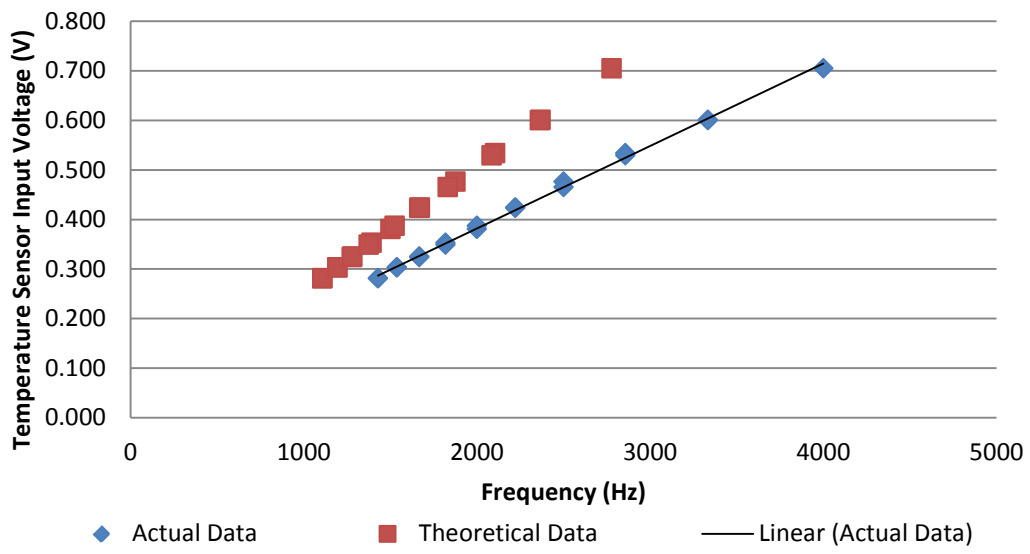


Figure 16. Actual and theoretical temperature sensor 1 data comparison.

Table 4. Temperature sensor 2.

| Temp Sensor Input Voltage (V) Run 1 | Temp Sensor Input Voltage (V) Run 2 | Measured Data | Theoretical Data |
|-------------------------------------|-------------------------------------|---------------|------------------|
| Period ( $\mu$ s)                   | Frequency (Hz)                      |               | Frequency (Hz)   |
| 700                                 | 1428.571                            | 1107.233      |                  |
| 650                                 | 1538.462                            | 1189.980      |                  |
| 600                                 | 1666.667                            | 1276.668      |                  |
| 550                                 | 1818.182                            | 1386.997      |                  |
| 500                                 | 2000.000                            | 1505.207      |                  |
| 450                                 | 2222.222                            | 1674.641      |                  |
| 400                                 | 2500.000                            | 1836.195      |                  |
| 350                                 | 2857.143                            | 2080.495      |                  |
| 300                                 | 3333.333                            | 2411.483      |                  |
| 250                                 | 4000.000                            | 2750.352      |                  |

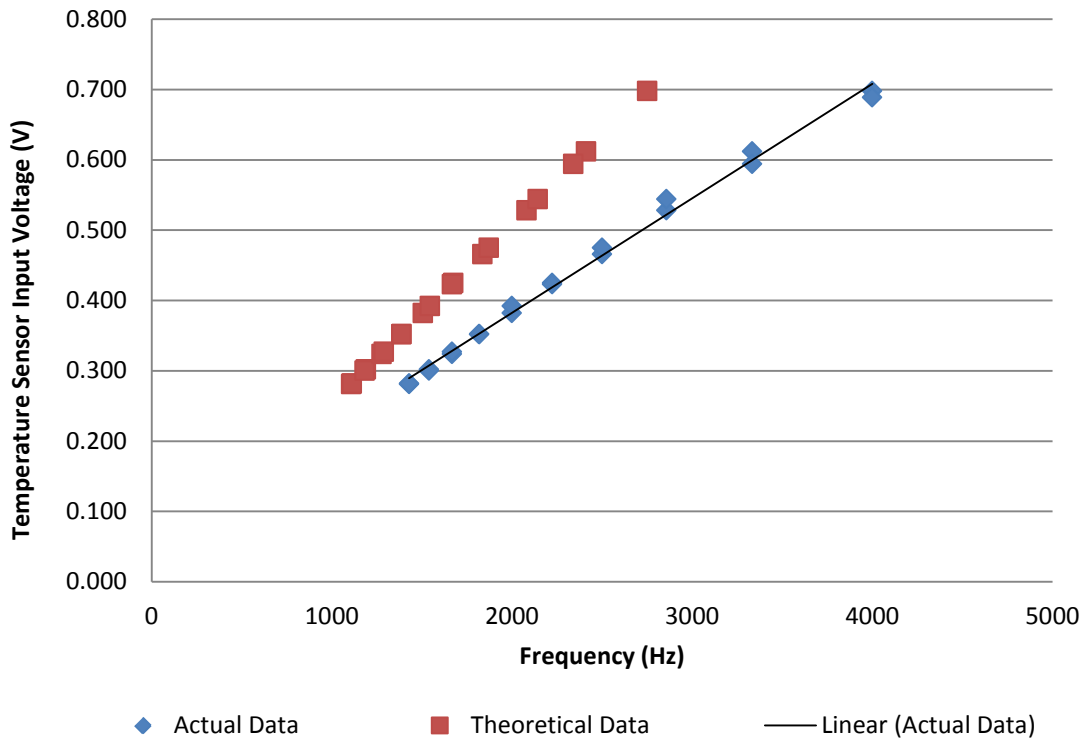


Figure 17. Actual and theoretical temperature sensor 2 data comparison.

Table 5. Sensor calibration data.

| Sensor                  | m      | b       | Correlation |
|-------------------------|--------|---------|-------------|
| Battery Voltage Board 1 | 0.0011 | -0.0645 | 0.9996      |
| Battery Voltage Board 2 | 0.0011 | 0.1806  | 0.9980      |
| Temperature Board 1     | 0.0002 | 0.0489  | 0.9981      |
| Temperature Board 2     | 0.0002 | 0.0570  | 0.9950      |

After taking temperature and voltage data for board 1 and board 2, we fit the actual data to a linear trend line for each sensor circuit. One observation, worth mentioning in Table 5, is that the calibration data is not the same for each circuit even though all of the components are the same. This is important to note because, in a manufacturing environment, calibrating every sensor for every board produced would be costly and time consuming. The most prudent solution is the development of automated software for calibration and is a good topic for future research.

## D. READING THE DIGITAL DATA

After the frequency-varying signal is created it must be digitized to represent the measured voltage or temperature. With optically isolated digital pulses input to the EMS, control logic can be designed to read the digital data for measurement, calibration, control and display within the FPGA of the EMS. The measurement and calibration logic is depicted in Figure 18. Larger versions of the same circuit are shown in Figure 19 and Figure 20 to provide better image resolution.

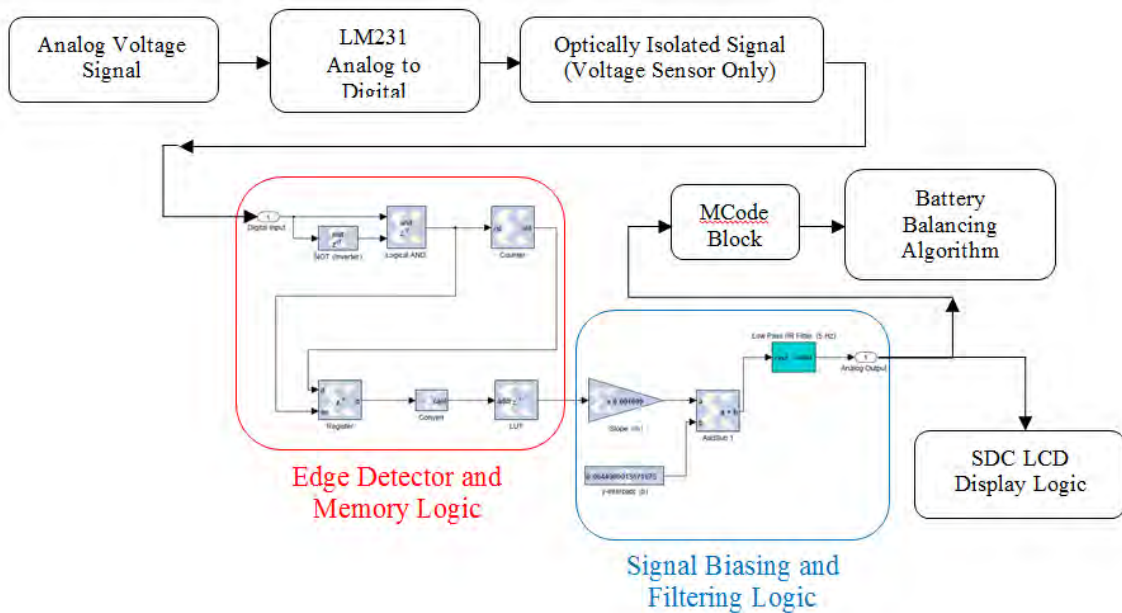


Figure 18. Signal flowchart.

The first step in converting the digital voltage signals back into useful data is to measure the frequency. Frequency measurement is accomplished with an edge detector. Combining the input rising edge digital data stream with an inverted and delayed version of the same signal creates an edge detector pulse that is one time step wide; the Simulink model runs with a 40 ns time step to represent the FPGA clock. With signal edges created, the clock cycles can be counted between rising edges to determine the value of the signal period. The number of clock cycles, which represents the period of the V-to-F signal, is stored in a register on the FPGA.

Now that the period of the digital signal has been measured, the signal can be processed for control and display. The inverse of the period is the frequency of the input signal. The first step in this process is to invert the period output from the register. This can be accomplished using many different block types within Simulink; however, most of the direct math operations are computationally intensive for the FPGA. The simplest solution is to create a lookup table (LUT), shown in Figure 19, which calculates the inverse of the period and stores the result in ROM.

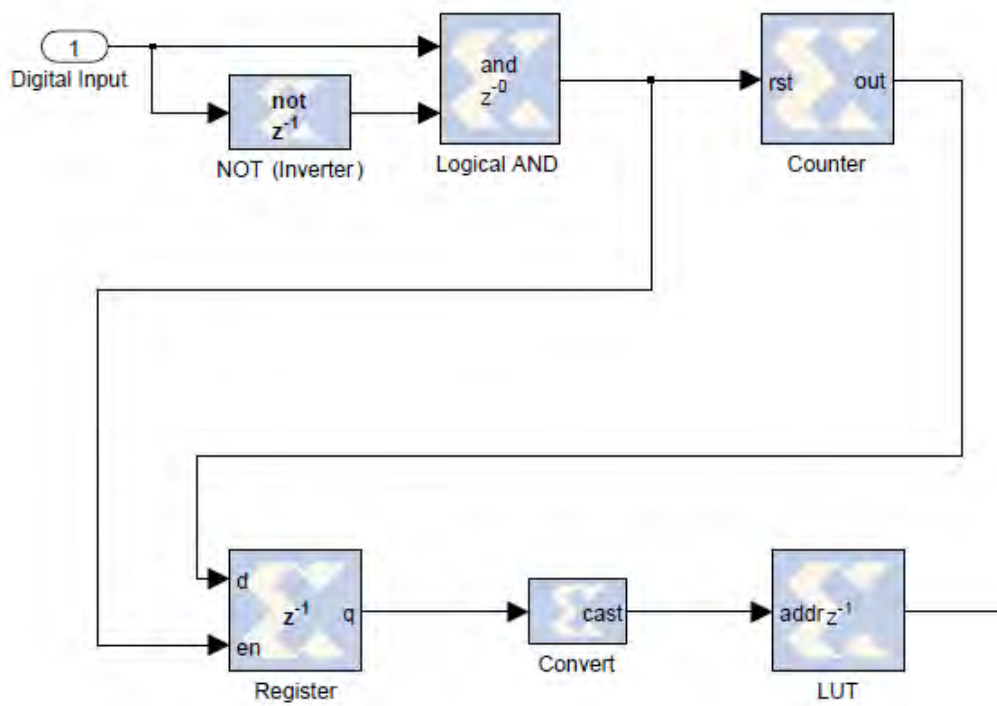


Figure 19. Edge detector and memory logic.

Subsequently, during operation, the program references the lookup table to convert the average period of the input data into a frequency. One solution to generating the lookup table involves programming the lookup table in the initial conditions file. The initial conditions file runs and builds the LUT when the Simulink model is executed.

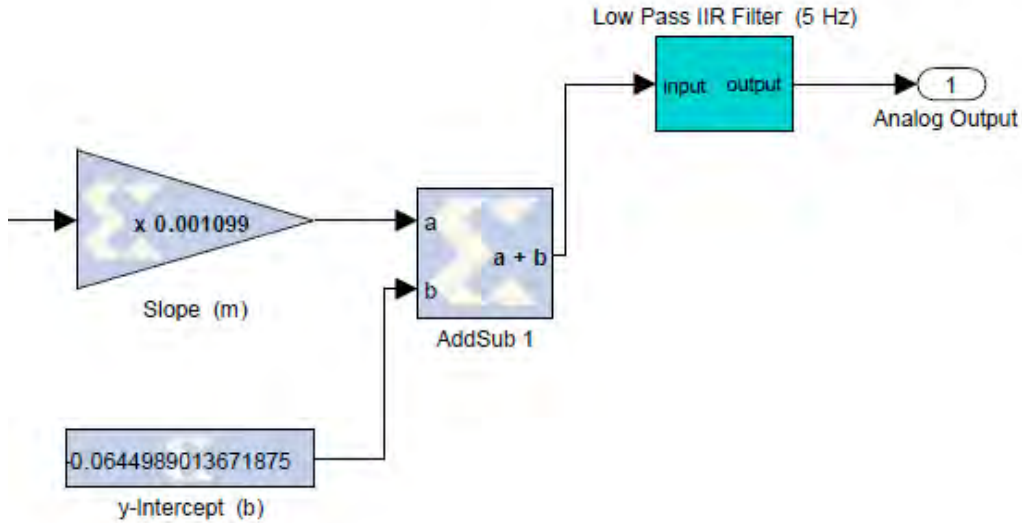


Figure 20. Signal biasing and filtering logic.

The goal of the signal processing circuit is to convert the signal data into the same format as the linearized representation of the calibration data trend line in Excel; the Simulink equivalent is shown in Figure 20. After converting the measured period data into its associated frequency, we use the linearized equation for calibration and display

$$V = fm + b \quad (3)$$

where  $V$  is a digitally processed version of the input measured voltage,  $f$  is the frequency converted from the LUT,  $m$  is the trend line slope and  $b$  is the  $y$ -intercept calculated by Excel. The specific sensor calibration data values are shown in Figure 14. To determine the slope of the data linearization, Excel uses regression analysis. The slope  $m$  of the trend line is calculated as

$$m = \frac{n \sum(xy) - \sum x \sum y}{n \sum(x^2) - \sum(x)^2} \quad (4)$$

where  $n$  is the number of data points,  $x$  represents the independent variable, and  $y$  represents the dependent variable [9]. The limits of the summation can be anything within the range of the data. In this case the trend line uses all the measured data, thus, the limits

of the summation are the entire data set. In addition to calculating the trend line slope, the y-intercept  $b$  is calculated as

$$b = \frac{\sum y - m \sum x}{n} \quad (5)$$

where  $n$  is the number of data points,  $x$  represents the independent variable,  $y$  represents the dependent variable, and the range of summation is the range of the data set [9]. When conducting regression analysis on a data set, it is important to investigate how close the measured data fits the representation, or trend line, chosen. This is most easily accomplished by measuring the correlation of the data to the trend line.

There are many important factors to consider when choosing a component for a system. The LM231 is chosen based on a few main considerations, namely, low power dissipation, wide dynamic range, low cost, and most importantly, a highly accurate linear output. The sensor data collected in the lab is input into Excel for analysis and graphing. Once the data is input, a linear trend line is fit to the data. Excel uses regression analysis to determine the data representation trend line equation. Since the linear trend line slope and intercept points are used to calibrate the system sensors, an assessment of the linearity of the actual data measurements is prudent. Excel's trend line function displays the square of the correlation coefficient  $R^2$  of the data. The value of the correlation coefficient  $R$  is based on the trend line chosen and is an indication of how accurately the data representation matches the data. The correlation coefficient is defined as

$$R = \frac{n \sum(xy) - \sum x \sum y}{\sqrt{[n \sum(x^2) - (\sum x)^2][n \sum(y^2) - (\sum y)^2]}} \quad (6)$$

where  $n$  is the number of data points,  $x$  represents the independent variable,  $y$  represents the dependent variable, and the range of summation is the range of the data set [9]. Since the actual data measurements are highly linear, the correlation coefficient and its squared value are very close to 1.0, which indicates a high level of correlation. Thus, our measured data fits the trend line chosen and is highly linear [9].

Given the measured values from the actual data trend line equation from Figure 14, the output of the ROM signal is multiplied by  $m$  to apply the appropriate amount of

gain. After the slope has been established, the signal is biased based on the trend line  $y$ -intercept point. After biasing, the signal is fully calibrated; however, testing reveals that high frequency transients were present on the output analog signal. To solve this, the signal is passed through a first order infinite impulse response (IIR) low pass filter, shown in Figure 21, to remove the high frequency transients in the output signal. The cutoff frequency of the low pass filter is set at 5 Hz. The transients can be attributed to noise on the line or bit errors in processing.

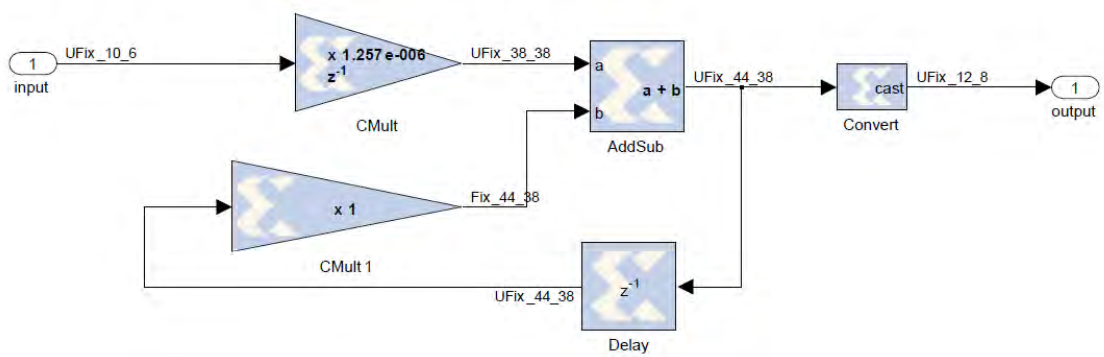


Figure 21. First order IIR low pass filter.

The operation of the low pass filter block shown in Figure 21 is based on the fundamental theorem of calculus, which is known as a Riemann Sum. An interval  $[a, b]$  is divided into  $n$  subintervals of equal width  $\Delta x$ , where

$$\Delta x = \frac{b-a}{n} \quad (7)$$

and

$$a = x_0 < x_1 < x_2 < \dots < x_n = b. \quad (8)$$

The definite integral of  $f$  over the interval  $[a, b]$  is

$$\int_a^b f(x)dx = \lim_{n \rightarrow \infty} \sum_{i=1}^n f(x_i^*)\Delta x, \quad (9)$$

where the right side of the equation is traditionally known as the Riemann sum of the function  $f$  over the interval  $[a, b]$ . The value  $n$  is the number of subintervals for the

approximation, and  $x_i^*$  can represent various values depending on the type of Riemann sum. There are three basic types of Riemann sum: a left Riemann sum, a right Riemann sum, and a middle Riemann sum. The symbolic notation for these three types of summation is

$$\begin{aligned} x_i^* &= x_{i-1} \\ x_i^* &= x_i \\ x_i^* &= \frac{1}{2}(x_i - x_{i-1}) \end{aligned} \quad (10)$$

where the delayed version represents the left Riemann sum, the present version represents the right Riemann sum and the last, symbolic representation finds the midpoint between the left and right Riemann sums [10].

The Xilinx blocks that comprise the low pass filter operate in a similar manner. In the Laplace domain, the transfer function for a first order low pass filter is

$$f(s) = \frac{\alpha}{s + \alpha} = \frac{y}{x} \quad (11)$$

which has a complex argument  $s$  and a constant value  $\alpha$ , which affects the pole and zero locations of the transfer function. The transfer function itself can also be represented as the output signal  $y$  divided by the input signal  $x$ . After some algebraic manipulation, Equation 11 can be rewritten as

$$y = \frac{1}{s} \alpha(x - y) \quad (12)$$

which has an equivalent time domain form of

$$y = \int \alpha(x - y) dt. \quad (13)$$

Since the model can only process discrete values, the continuous time integration must be rewritten into a discrete time digital approximation. It can be shown from Equation 13 that the discrete approximation of the transfer function is

$$y_{k-1} = -\alpha(x_{k-1} - y_k)\Delta t \quad (14)$$

or

$$y_{k-1} = y_k(1 - \alpha\Delta t) + x_k(\alpha\Delta t) \quad (15)$$

where the output value of the filter is  $y_{k-1}$ . The values  $y_k$  and  $x_k$  represent the previous state output and input values, respectively. The value of  $\alpha$  remains a constant associated with the poles and zeros of the transfer function, and  $\Delta t$  represents the time step, which is synonymous with  $\Delta x$  in the Riemann sum. To translate Equation (14) into Simulink is fairly straightforward. The input to the low pass filter is represented by  $x_k$ . The output of the low pass filter is represented by  $y_{k-1}$ , and similarly the previous value of the output is represented by  $y_k$ . The value for  $\Delta t$  is established in the initial conditions file of the Simulink model and is named *tstep*, with a constant value of 40 ns. The value of  $\alpha$  is represented in the Simulink blocks in the gain values for *CMult* and *CMult1*. The constant  $\alpha$  is

$$\alpha = 2\pi f_{low}. \quad (16)$$

The initial gain block, labeled *CMult*, increases the input signal by a predefined constant value, where *CMult* is defined as

$$CMult = 2\pi f_{low}tstep \quad (17)$$

where  $f_{low}$  is a constant of 5 Hz, which sets the cutoff frequency of the filter and is established in the initial conditions file of the model. Additionally, *tstep* is a constant of 40 ns which is defined in the initial conditions file and sets the time step for the model.

The signal then passes through an adder block which combines the output of the *CMult* block with a delayed version of the same signal. The delayed signal is passed through another gain block, labeled *CMult1*, where *CMult1* is defined as

$$CMult1 = 1 - 2\pi f_{low}tstep \quad (18)$$

The combination of the delayed signal and the input signal through the use of the adder allows the blocks to sum values of the input signal over the interval of runtime in the

model. The *tstep* value is analogous to  $\Delta x$  in the Riemann sum. As the value for *tstep* increases, the accuracy of the integration increases but causes the model to run slower. This highlights a tradeoff that must be made between accuracy and processing speed when choosing the time step value. By choosing a reasonably small time step value, the model will achieve acceptable accuracy without incurring an impractical degradation in simulation time.

The range of frequencies generated by the LM231 is an important factor depending on the application. The LM231 is designed to operate over a frequency range of 1.0 Hz to 100 kHz [7]. The circuit is calibrated to read frequency signals around 10 kHz. This is important to mention because the data rate of the signal pulses directly affects the time response of the control circuitry. This can be significant, depending on the application of the control algorithm. In this case, a rapid time response is not vital because the voltage signals are not expected to change rapidly during operation. If the rate of change of the input signal did have a fast time response, analysis of the minimum data rate required to achieve control or protective action would be required. One solution to this problem would be the establishment of a threshold value, which prevents the input parameter from reaching an unsafe level based on the expected rate of change of the input signal.

THIS PAGE INTENTIONALLY LEFT BLANK

### III. DESIGN OF THE BATTERY BALANCING CONTROL ALGORITHM

#### A. BACKGROUND

There are numerous control methodologies that can be utilized to balance a battery string. In many passive charging topologies, resistors are used between cells to balance the voltage between the highest and lowest cells. Other arrangements use transformers or various switching layouts to transfer power and balance the string. The active charging methodology being developed at NPS around the EMS utilizes a stack charger to bulk charge the string and individual cell SLR converters to preferentially trickle charge each cell [11]. The main benefit of this arrangement is efficiency and flexible control. Efficiency gains are realized through the employment of SLR converters. When SLR converters operate in discontinuous conduction mode, switching losses are minimized during power transfer [12]. Additionally, by programming the individual cell chargers to only turn on when a low state of charge is sensed, the main power transfer occurs through the stack charger, shown in Figure 22. By concentrating the majority of the power transfer through a large bulk charger, the size of the individual SLR converters can be minimized, which minimizes component costs.

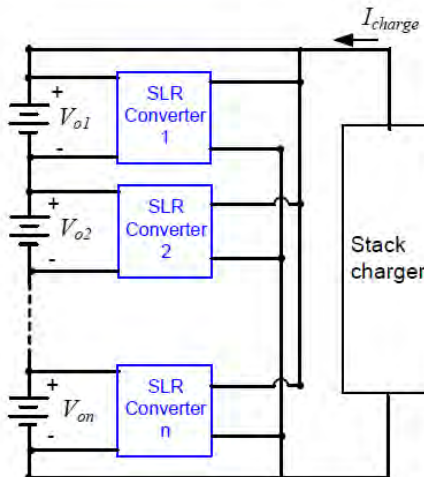


Figure 22. Multicell battery stack setup. From [11].

## B. DESIGNING THE BATTERY BALANCING ALGORITHM

In addition to the efficiency gains realized through power converter topology, system control flexibility is provided by using Simulink in conjunction with the Xilinx software to design the control architecture. By using a software based platform, we can integrate the system hardware with the software in Xilinx. Once all of the appropriate pin locations have been identified and programmed for temperature and voltage sensing, control signals can be sent to turn on and turn off each individual charger. With a fully integrated system, the control algorithm can be developed in a number of different ways. The control algorithm to determine which battery should be charged is shown in Figure 23. The algorithm finds the cell with the lowest voltage and charges it if the cell voltage is below the full charge threshold. With voltage thresholds established, the algorithm associates predefined control signal variables to each cell which are then toggled to true or false based on the voltage threshold input by each battery cell. For clarity, the control signals in Figure 23 have been named  $V_{1,\text{control}}$  and  $V_{2,\text{control}}$ . To further explain the nomenclature, if the battery string had  $n$  battery cells and associated SLR charger control signals, then the control signal for the  $n^{\text{th}}$  cell would be labeled  $V_{n,\text{control}}$ , where  $n$  denotes the cell number associated with each battery cell in the series connected string.

At the most basic level, most of the balancing algorithms center on sensing the state of charge, which is directly proportional to cell voltage from 20 percent to 90 percent of total charge [5]. Then, the algorithm must determine which cell in the battery string has the lowest voltage and trigger the associated SLR converter to charge to that cell. A visual representation of the control algorithm written for this research is depicted in Figure 23.

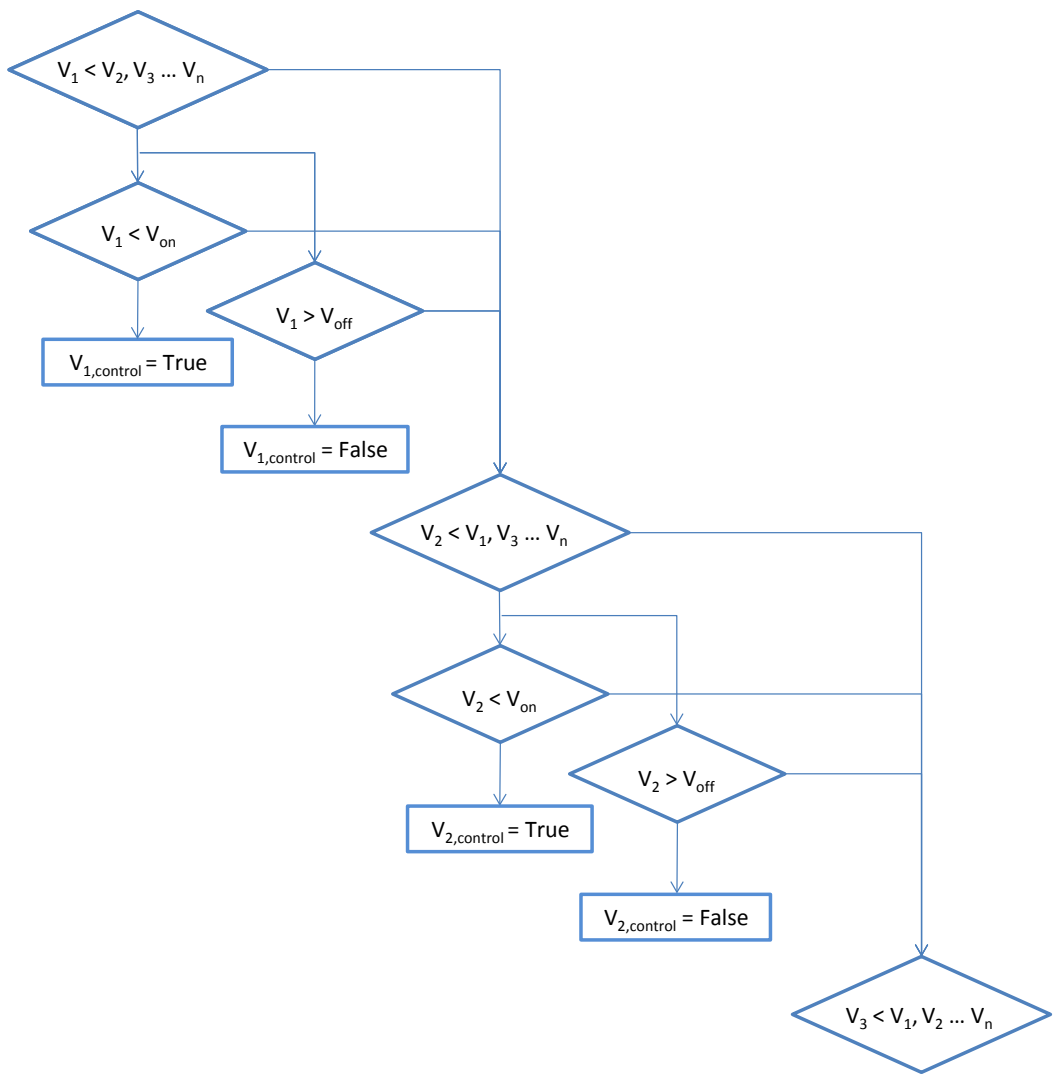


Figure 23. Battery balancing control logic.

The algorithm receives voltage input from each individual cell voltage sensor and compares the voltage of that cell with all of the other cells in the string. It then identifies which cell has the lowest voltage, and if that voltage is lower than a specified individual cell low set point, the control signal is toggled to true and is sent to the associated individual cell SLR converter. The control signal remains true, and the individual cell is charged until the associated voltage reaches a specified high set point. It is important to

note that the low-on set point and the high-off set point must be set at different thresholds to prevent excessive hunting and maintain system hysteresis.

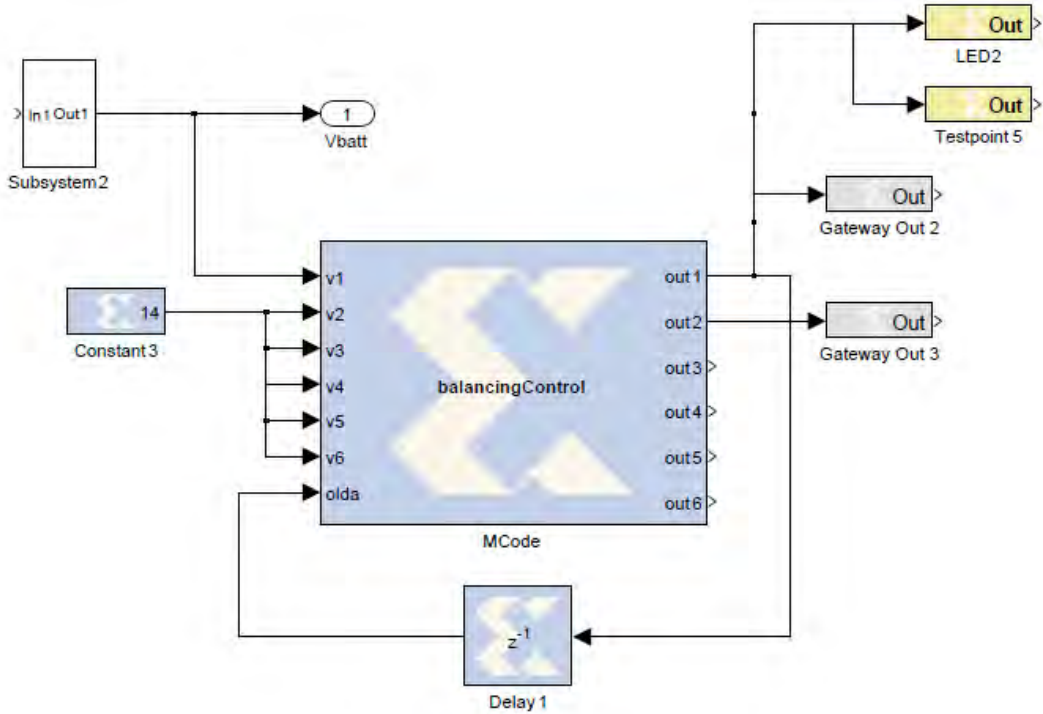


Figure 24. Battery cell balancing control circuit.

The threshold of the on and off signals was initially set to turn on at 11.5 V and turn off at 12 V. These levels were arbitrary, but a hysteresis band between the high and low set points is essential. In this case, a 0.5 V hysteresis was chosen and set in the system to prove the control concept in Simulink and later on the visual display of the EMS. Lower hysteresis values proved to be too sensitive to control while taking photos of the laboratory setup. In reality the hysteresis band must be set once system operation has been observed. Of course the main goal is to minimize short cycling the SLR converters while maintaining the entire string around the 12 V operating range.

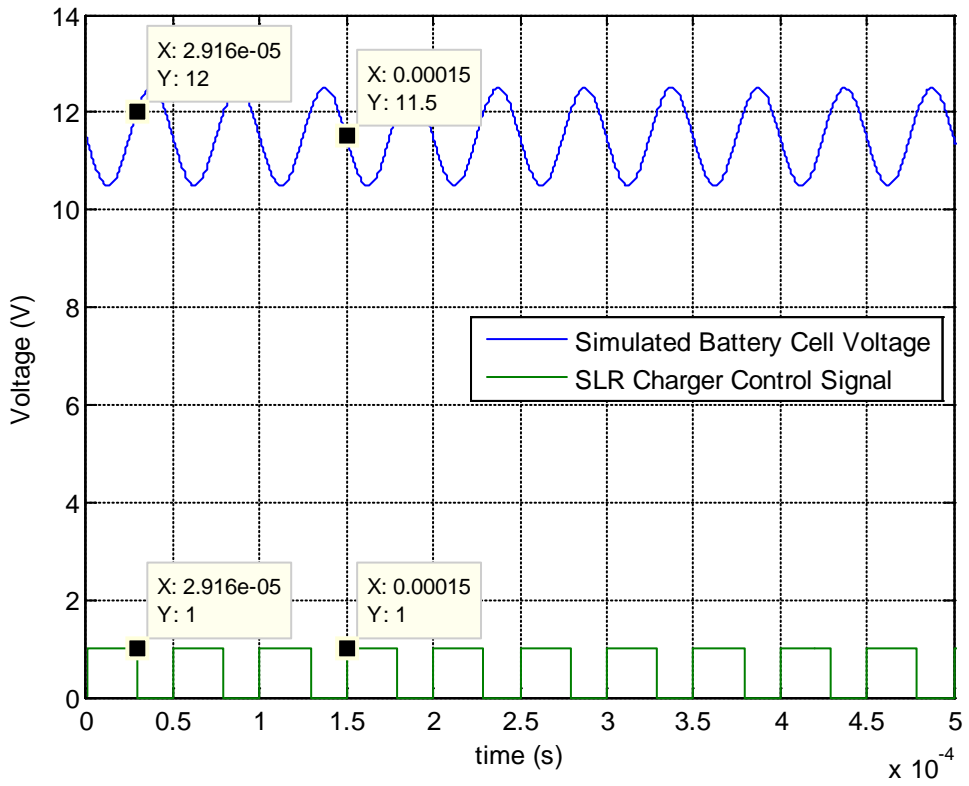


Figure 25. Simulated individual battery cell voltage and associated control signal.

Once the script file, shown in Appendix A, for the control algorithm is written, the individual cell voltages must be connected so that the script file will read the individual cell voltages and operate as designed. This is accomplished in Xilinx by using an MCode block, which calls a file in the same directory as the power converter model. In this case, the MCode block calls the battery balancing algorithm MATLAB script. The Xilinx to script file interface is shown in Figure 24. It is important to note the battery voltages for cells one through six were set at a constant value of 14 V for testing within the model to validate that the model operates as designed prior to conversion and upload to the FPGA. To demonstrate the system operation within the system model, the number one voltage cell is set, within Subsystem 2, as a sine wave and control signals are observed at the output of the MCode block. The results, which validate the design, are plotted in Figure 25. Proper operation of the battery balancing algorithm is demonstrated based on the  $x$ -values of the data cursors, which represent time, in Figure 25. The first

pair of cursors, with a time value of 0.2916  $\mu$ s, shows that the control signal turns off when the input voltage rises above 12 V. The second pair of cursors, with a time value of 150  $\mu$ s, shows that the control signal turns on when the input voltage decreases below 11.5 V. The threshold values of 12 V and 11.5 V were chosen for clarity in validating the model but can be set to any user desired value. The final values chosen are developed by experimental analysis and are an area for future research.

Once the operation of the control algorithm is demonstrated in the Simulink model, the software is converted to very high speed integrated circuits (VHSIC), VHSIC hardware description language (VHDL) code [13]. This is accomplished using the ISE Design Suite for Xilinx, a Xilinx proprietary program which converts the modified EMS Simulink model and embedded Xilinx digital signal processing (DSP) blocks into machine readable code for the EMS FPGA. Once the VHDL version of the EMS model and controller has been built, the code is loaded on the FPGA using Chipscope Pro, another Xilinx proprietary program. Pictures of the LCD on the control card of the EMS are shown in Figure 26 and Figure 27 and are used to demonstrate the proper operation of the battery balancing system by indicating the battery voltage threshold and the status of LED2.



Figure 26. Individual cell voltage and SLR charger control ON signal.

Now that the EMS control software has been loaded on the FPGA, the expected operation of the system can be verified on the hardware. To test that the control signal generated by the battery balancing system is working properly, a light emitting diode (LED) block is connected in the Simulink model to the output control signal for the number one battery cell SLR changer. This Xilinx DSP block maps to the number 2 LED on the EMS development board and is low enabled, which is set by the manufacturer of the development board that the EMS is designed around [14].

There is a red arrow pointing at LED2. The measured battery voltage  $V_{batt}$  is displayed and was verified to match the V-to-F input voltage. The LED2 is off when the system is set to charge, and LED2 turns on when charging stops. The signal input to LED2 is the same signal associated with the SLR charger control signal. Since the LED is set to low enabled, when a low signal is received during operation, the LED is on. The expected and demonstrated system response is that the LED is off when the SLR charger receives a true (on) signal at a  $V_{batt}$  value below 11.5 V, shown in Figure 26, and the LED is on when the SLR charger receives a false (off) signal at a  $V_{batt}$  value above 12 volts, shown in Figure 27.



Figure 27. Individual cell voltage and SLR charger control OFF signal.

THIS PAGE INTENTIONALLY LEFT BLANK

## **IV. CONCLUSIONS AND RECOMMENDATIONS**

### **A. OBSERVATIONS AND FUTURE WORK**

After taking temperature and voltage data for board 1 and board 2, the actual data were fit to a linear trend line for each sensor circuit. One observation worth mentioning in Table 5 is that the calibration data is not the same for each circuit even though all of the components are the same. This is important to note because, in a manufacturing environment, having to calibrate every sensor for every board produced would be costly and time consuming. The most prudent solution is the development of automated software for calibration and is a good topic for future research.

### **B. CONCLUSION**

The advantage of designing a power storage, conversion, and battery management system around microprocessor based control is the flexibility it provides. As the systems are developed and operated, more and more data will be gathered about the batteries. This material history will provide vital insight into future advances in control methodologies. Additionally, due to the flexibility of the EMS system and the microprocessor based control algorithm, as advances in battery technology are discovered, small software changes will enable the system to operate in a more dynamic manner with no hardware change. As comparable systems enter the market, more battery data will become available. The future story of battery strings and power converters will be similar to the story of the internal combustion engine. Although the technology has been in existence for more than a century, advances in engine technology have continued to yield efficiency savings in our modern world. Battery technology is at a similar tipping point. Market solutions are available for consumer based energy storage, but there are a wide variety of changes that will help advance the technology. One day our energy storage systems will be web enabled, allowing state of charge data to be logged, which will provide consumers and industry with more data to further optimize their systems. As we continue to advance the chemistry of battery cell type, we will have to continue to advance battery control algorithms to provide safe and optimized operation. One day our

systems will be so advanced that mismatches in battery lifetime and type will have little impact on safety and efficiency.

## APPENDIX A. BATTERY BALANCING ALGORITHM

```
function [out1, out2, out3, out4, out5, out6] = balancingControl(v1,
v2, v3, v4, v5, v6,olda)
% This function returns the char codes for the voltage
% to be displayed in the LCD

out1a=olda
out2a=olda
out3a=olda
out4a=olda
out5a=olda
out6a=olda

Von=xfix({xlUnsigned, 12, 9}, 11.5);
Voff=xfix({xlUnsigned, 12, 9}, 12.0);

if v1 < v2, v3, v4, v5, v6;
if v1 < Von
    out1a=true;
end
end

if v1 > Voff
    out1a=false;
end

if v2 < v1, v3, v4, v5, v6;
if v2 < Von
    out2a=true;
end
end

if v2 > Voff
    out2a=false;
end

if v3 < v1, v2, v4, v5, v6;
if v3 < Von
    out3a=true;
end
end

if v3 > Voff
    out3a=false;
end

if v4 < v1, v2, v3, v5, v6;
if v4 < Von
    out4a=true;
end
end
```

```

if v4 > Voff
    out4a=false;
end

if v5 < v1, v2, v3, v4, v6;
if v5 < Von
    out5a=true;
end
end

if v5 > Voff
    out5a=false;
end

if v6 < v1, v2, v3, v4, v5;
if v6 < Von
    out6a=true;
end
end

if v6 > Voff
    out6a=false;
end
out1=xfix({xlBoolean},out1a);
out2=xfix({xlBoolean},out2a);
out3=xfix({xlBoolean},out3a);
out4=xfix({xlBoolean},out4a);
out5=xfix({xlBoolean},out5a);
out6=xfix({xlBoolean},out6a);

```

## APPENDIX B. INITIAL CONDITIONS FILE

```

pulsect=1800;
tstep = 40e-9;

% f_low=5*40;      %cutoff for rms filters set to 5 hz
% f_high=350*8;  %cutoff for LPF on AC input set to 350 hz
% start_record=round(2/12000/tstep);
% fin=60*20;    % change to 60 hz used in PLL
% finb=60*20*1.5; % change to 60 hz used in PLL

f_low=5;      %cutoff for rms filters set to 5 hz

f_high=350; %cutoff for LPF on AC input set to 350 hz
start_record=round(2/60/tstep);
fin=60;    % change to 60 hz used in PLL
finb=60;   % change to 60 hz used in PLL

Kp_i_boost=.05;
Ki_i_boost=20;

%%%%%%%%%%%%% Stator side config
%%%%%%%%%%%%%
f_clock=25e6;
sw_freq=15000;
sw_counter=round(f_clock/sw_freq-mod(f_clock/sw_freq,10)); %Counter
for sawtooth for switching modulo 10 used so step_ct can be 10
Vdc=160;
V_phase=sqrt(2)*120;    %%120V for rotor ckt...60V for stator ckt
(variac)
Ks=2/3*[1 -1/2 -1/2;0 -sqrt(3)/2 sqrt(3)/2;1/2 1/2 1/2];    %abc to qd0
transformation in the stationary frame
f_fund = 60;
omega_b = 2*pi*60;
oversample=2;
%%%%%%%%%%%%% step_ct= 1 %%%%%%
%%%%%%%%%%%%%

tstop=4;

%%%%%%%%%%%%%Stator PI Gains%%%%%%%%%%%%%
Kp_vdc=.02*2;
Ki_vdc=.002*3;

Kp_i_s=20/3;
Ki_i_s=10;
%%%%%%%%%%%%%
Lf=300e-6;
Rf=.05;

```

```

%
twopiby3 = 2*pi/3;
poles = 4;
polesby2J=poles/2/(.089); % .0024 kg/m^2 per labvolt spec sheet
TL=200/(2/poles*omega_b);

% %%%%%%%%%%%%%%Rotor Speed/Current PI
Gains%%%%%%%%%%%%%
Kp_i=80/5;
Ki_i=100/50;

%
%%%%%%%%%%%%%
%%

rs=12;
rr = 4;
Xls =9;
Xm =180;
Xlr = 9;

D=(Xls+Xm)*(Xlr+Xm)-Xm^2;
rsbyXls = rs/Xls;
rrbyXlr = rr/Xlr;
Xaq = 1/(1/Xm+1/Xls+1/Xlr);
Xad = Xaq;
XaqbyXls = Xaq/Xls;
XaqbyXlr = Xaq/Xlr;
XadbyXls = Xad/Xls;
XadbyXlr = Xad/Xlr;
XaqbyXm = Xaq/Xm;
XadbyXm = Xad/Xm;
psi_qsic=0;
psi_dsic=0;
psi_qric=0;
psi_dric=0;
omegar_ic = omega_b;
Kp_iqs=50;
Ki_iqs=.1;
Kp_iqr=50;
Ki_iqr=.1;
F_mat = [ 0 0 0 1;1 1 2 0;2 2 3 0;3 3 0 0];
O_mat = F_mat;

%%%%%%%%%%%%%
%%%
gain1=1/(1/3000+1/200000)/(1/(1/3000+1/200000)+56000*2);
gain2=1/(1/6800+1/200000)/(1/(1/6800+1/200000)+120000*2); %DC sensor
gain
gainI=3/1000*330; %current sensor gain resistor is 330 ohms
gainI220=3/1000*220; %current sensor gain resistor is 220 ohms in new
boards

```

```

% 9 bits are [r/s d7 d6 ... d0]
LCD_data=[ ...
bin2dec('000110000');...      %
bin2dec('000110000');...
bin2dec('000110000');...
bin2dec('000110000');...
bin2dec('000111100');...      % 2 lines 5:10 dot resolution
bin2dec('000001110');...
bin2dec('000000001');...
bin2dec('000000110');...
bin2dec('1')*2^8+hex2dec('4e');... %N
bin2dec('1')*2^8+hex2dec('50');... %P
bin2dec('1')*2^8+hex2dec('53');... %S
bin2dec('1')*2^8+hex2dec('20');... % space
bin2dec('1')*2^8+hex2dec('45');... %E
bin2dec('1')*2^8+hex2dec('4d');... %M
bin2dec('1')*2^8+hex2dec('53');... %S
bin2dec('1')*2^8+hex2dec('20');... % space

bin2dec('011000000');...      % set AC to second line
bin2dec('1')*2^8+hex2dec('74');... %t
bin2dec('1')*2^8+hex2dec('65');... %e
bin2dec('1')*2^8+hex2dec('73');... %s
bin2dec('1')*2^8+hex2dec('74');... %t
bin2dec('1')*2^8+hex2dec('20');... %space
bin2dec('1')*2^8+hex2dec('20');... %space
bin2dec('1')*2^8+hex2dec('20');... %space
bin2dec('1')*2^8+hex2dec('4e');... %N
bin2dec('1')*2^8+hex2dec('50');... %P
bin2dec('1')*2^8+hex2dec('53');... %S
bin2dec('1')*2^8+hex2dec('20');... % space
bin2dec('1')*2^8+hex2dec('45');... %E
bin2dec('1')*2^8+hex2dec('4d');... %M
bin2dec('1')*2^8+hex2dec('53');... %S
bin2dec('1')*2^8+hex2dec('20');... % space
];

LCD_data2=[ ...
bin2dec('011000000');...      % set AC to second line
bin2dec('1')*2^8+hex2dec('56');... %V
bin2dec('1')*2^8+hex2dec('64');... %d
bin2dec('1')*2^8+hex2dec('63');... %c
bin2dec('1')*2^8+hex2dec('3d');... %=
bin2dec('1')*2^8+hex2dec('20');... % space
bin2dec('1')*2^8+hex2dec('4e');... % voltage displayed
bin2dec('1')*2^8+hex2dec('4e');... % voltage displayed
bin2dec('1')*2^8+hex2dec('20');... % voltage displayed
bin2dec('1')*2^8+hex2dec('20');... % space
bin2dec('1')*2^8+hex2dec('76');... %v
bin2dec('1')*2^8+hex2dec('6f');... %o
bin2dec('1')*2^8+hex2dec('6c');... %l
bin2dec('1')*2^8+hex2dec('74');... %t
bin2dec('1')*2^8+hex2dec('73');... %s
bin2dec('1')*2^8+hex2dec('20');... % space

```

```

bin2dec('010000000');... % set AC to first line
bin2dec('1')*2^8+hex2dec('56');... %V
bin2dec('1')*2^8+hex2dec('62');... %b
bin2dec('1')*2^8+hex2dec('61');... %a
bin2dec('1')*2^8+hex2dec('74');... %t
bin2dec('1')*2^8+hex2dec('74');... %t
bin2dec('1')*2^8+hex2dec('3d');... %=
bin2dec('1')*2^8+hex2dec('4e');... % current displayed
bin2dec('1')*2^8+hex2dec('4e');... % current displayed
bin2dec('1')*2^8+hex2dec('2e');... % .
bin2dec('1')*2^8+hex2dec('4e');... % current displayed
bin2dec('1')*2^8+hex2dec('20');... % space
bin2dec('1')*2^8+hex2dec('56');... %V
bin2dec('1')*2^8+hex2dec('44');... %D
bin2dec('1')*2^8+hex2dec('43');... %C
bin2dec('1')*2^8+hex2dec('21');... %!
];

Lres=35e-6;
Cres=23e-9;
fres=1/2/pi/sqrt(Lres*Cres)
tres=1/fres
res_ct=round(tres/tstep)
on_ct=round(tres/tstep*.7)

%%%%%%%%%%%%%%%
%Voltage Sensor LUT
Index=[1:2^12];
reciprocal=1/tstep./Index;

```

## **APPENDIX C. LM231 DATA SHEET**

This appendix contains the data sheet for the LM231 [7]. It details the operating parameters of the chip and the chip's design features.



National Semiconductor

June 1999

## LM231A/LM231/LM331A/LM331 Precision Voltage-to-Frequency Converters

### LM231A/LM231/LM331A/LM331 Precision Voltage-to-Frequency Converters

#### General Description

The LM231/LM331 family of voltage-to-frequency converters are ideally suited for use in simple low-cost circuits for analog-to-digital conversion, precision frequency-to-voltage conversion, long-term integration, linear frequency modulation or demodulation, and many other functions. The output when used as a voltage-to-frequency converter is a pulse train at a frequency precisely proportional to the applied input voltage. Thus, it provides all the inherent advantages of the voltage-to-frequency conversion techniques, and is easy to apply in all standard voltage-to-frequency converter applications. Further, the LM231A/LM331A attain a new high level of accuracy versus temperature which could only be attained with expensive voltage-to-frequency modules. Additionally the LM231/331 are ideally suited for use in digital systems at low power supply voltages and can provide low-cost analog-to-digital conversion in microprocessor-controlled systems. And, the frequency from a battery powered voltage-to-frequency converter can be easily channeled through a simple photoisolator to provide isolation against high common mode levels.

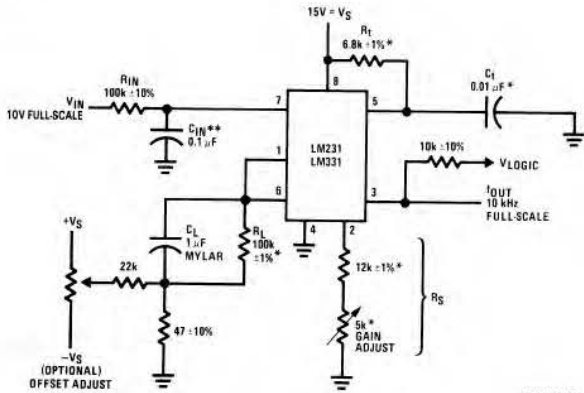
The LM231/LM331 utilize a new temperature-compensated band-gap reference circuit, to provide excellent accuracy

over the full operating temperature range, at power supplies as low as 4.0V. The precision timer circuit has low bias currents without degrading the quick response necessary for 100 kHz voltage-to-frequency conversion. And the output are capable of driving 3 TTL loads, or a high voltage output up to 40V, yet is short-circuit-proof against V<sub>CC</sub>.

#### Features

- Guaranteed linearity 0.01% max
- Improved performance in existing voltage-to-frequency conversion applications
- Split or single supply operation
- Operates on single 5V supply
- Pulse output compatible with all logic forms
- Excellent temperature stability,  $\pm 50 \text{ ppm}/^\circ\text{C}$  max
- Low power dissipation, 15 mW typical at 5V
- Wide dynamic range, 100 dB min at 10 kHz full scale frequency
- Wide range of full scale frequency, 1 Hz to 100 kHz
- Low cost

#### Typical Applications



$$f_{\text{OUT}} = \frac{V_{\text{IN}}}{2.09 \text{ V}} \cdot \frac{R_S}{R_L} \cdot \frac{1}{R_1 C_1}$$

\*Use stable components with low temperature coefficients. See Typical Applications section.

\*\*0.1μF or 1μF. See "Principles of Operation."

FIGURE 1. Simple Stand-Alone Voltage-to-Frequency Converter with  $\pm 0.03\%$  Typical Linearity ( $f = 10 \text{ Hz to } 11 \text{ kHz}$ )

Teflon® is a registered trademark of DuPont

## Absolute Maximum Ratings (Note 1)

If Military/Aerospace specified devices are required, please contact the National Semiconductor Sales Office/Distributors for availability and specifications.

|   | LM231A/LM231   | LM331A/LM331                           |
|---|--|--|
| Supply Voltage  | 40V  | 40V                                    |
| Output Short Circuit to Ground  | Continuous   | Continuous                             |
| Output Short Circuit to $V_{CC}$  | Continuous   | Continuous                             |
| Input Voltage   | -0.2V to + $V_S$                                       | -0.2V to + $V_S$                       |
| Operating Ambient Temperature Range   | $T_{MIN}$ to $T_{MAX}$<br>-25°C to +85°C               | $T_{MIN}$ to $T_{MAX}$<br>0°C to +70°C |
| Power Dissipation ( $P_D$ at 25°C) and Thermal Resistance ( $\theta_{JA}$ ) | (N Package) $P_D$<br>$\theta_{JA}$<br>1.25W<br>100°C/W | 1.25W<br>100°C/W                       |
| Lead Temperature (Soldering, 10 sec.)                                       | 260°C  | 260°C                                  |
| Dual-In-Line Package (Plastic)  |  |  |
| ESD Susceptibility (Note 4)   |  |  |
| N Package   | 500V   | 500V                                   |

## Electrical Characteristics

$T_A = 25^\circ C$  unless otherwise specified (Note 2)

| Parameter   | Conditions   | Min          | Typ                  | Max                   | Units            |
|---|--|--------------|----------------------|-----------------------|------------------|
| VFC Non-Linearity (Note 3)  | $4.5V \leq V_S \leq 20V$                                   |              | $\pm 0.003$          | $\pm 0.01$            | % Full-Scale     |
|   | $T_{MIN} \leq T_A \leq T_{MAX}$                            |              | $\pm 0.006$          | $\pm 0.02$            | % Full-Scale     |
| VFC Non-Linearity<br>In Circuit of Figure 1                               | $V_S = 15V$ , $f = 10$ Hz to 11 kHz                        |              | $\pm 0.024$          | $\pm 0.14$            | % Full-Scale     |
| Conversion Accuracy Scale Factor (Gain)<br>LM231, LM231A<br>LM331, LM331A | $V_{IN} = -10V$ , $R_S = 14 k\Omega$                       | 0.95<br>0.90 | 1.00<br>1.00         | 1.05<br>1.10          | kHz/V<br>kHz/V   |
| Temperature Stability of Gain<br>LM231/LM331<br>LM231A/LM331A             | $T_{MIN} \leq T_A \leq T_{MAX}$ , $4.5V \leq V_S \leq 20V$ |              | $\pm 30$<br>$\pm 20$ | $\pm 150$<br>$\pm 50$ | ppm/°C<br>ppm/°C |
| Change of Gain with $V_S$   | $4.5V \leq V_S \leq 10V$<br>$10V \leq V_S \leq 40V$        |              | 0.01<br>0.006        | 0.1<br>0.06           | %/V<br>%/V       |
| Rated Full-Scale Frequency  | $V_{IN} = -10V$  | 10.0         |                      |                       | kHz              |
| Gain Stability vs Time<br>(1000 Hrs)                                      | $T_{MIN} \leq T_A \leq T_{MAX}$                            |              | $\pm 0.02$           |                       | % Full-Scale     |
| Overrange (Beyond Full-Scale) Frequency                                   | $V_{IN} = -11V$  | 10           |                      |                       | %                |
| <b>INPUT COMPARATOR</b>   |  |              |                      |                       |                  |
| Offset Voltage<br>LM231/LM331<br>LM231A/LM331A                            | $T_{MIN} \leq T_A \leq T_{MAX}$                            |              | $\pm 3$<br>$\pm 4$   | $\pm 10$<br>$\pm 14$  | mV               |
|   | $T_{MIN} \leq T_A \leq T_{MAX}$                            |              | $\pm 3$              | $\pm 10$              | mV               |
| Bias Current  |  |              | -80                  | -300                  | nA               |
| Offset Current  |  |              | $\pm 8$              | $\pm 100$             | nA               |
| Common-Mode Range   | $T_{MIN} \leq T_A \leq T_{MAX}$                            | -0.2         |                      | $V_{CC} - 2.0$        | V                |
| <b>TIMER</b>  |  |              |                      |                       |                  |
| Timer Threshold Voltage, Pin 5  |  | 0.63         | 0.667                | 0.70                  | $x V_S$          |
| Input Bias Current, Pin 5<br>All Devices<br>LM231/LM331<br>LM231A/LM331A  | $V_S = 15V$  |              |                      |                       |                  |
|   | $0V \leq V_{PIN\ 5} \leq 9.9V$                             |              | $\pm 10$             | $\pm 100$             | nA               |
|   | $V_{PIN\ 5} = 10V$   |              | 200                  | 1000                  | nA               |
|   | $V_{PIN\ 5} = 10V$   |              | 200                  | 500                   | nA               |

## Electrical Characteristics (Continued)

$T_A=25^\circ\text{C}$  unless otherwise specified (Note 2)

| Parameter   | Conditions  | Min                      | Typ                        | Max                      | Units                   |
|---|---|--------------------------|----------------------------|--------------------------|-------------------------|
| <b>TIMER</b>  |   |                          |                            |                          |                         |
| $V_{SAT\ PIN\ 5}$ (Reset)   | $I = 5\text{ mA}$   |                          | 0.22                       | 0.5                      | V                       |
| <b>CURRENT SOURCE (Pin 1)</b>   |   |                          |                            |                          |                         |
| Output Current<br>LM231, LM231A<br>LM331, LM331A                          | $R_S=14\text{ k}\Omega$ , $V_{PIN\ 1}=0$  | 126<br>116               | 135<br>136                 | 144<br>156               | $\mu\text{A}$           |
| Change with Voltage   | $0\text{V} \leq V_{PIN\ 1} \leq 10\text{V}$   |                          | 0.2                        | 1.0                      | $\mu\text{A}$           |
| Current Source OFF Leakage<br>LM231, LM231A, LM331, LM331A<br>All Devices | $T_A=T_{MAX}$   |                          | 0.02<br>2.0                | 10.0<br>50.0             | nA                      |
| Operating Range of Current (Typical)                                      |   |                          | (10 to 500)                |                          | $\mu\text{A}$           |
| <b>REFERENCE VOLTAGE (Pin 2)</b>  |   |                          |                            |                          |                         |
| LM231, LM231A<br>LM331, LM331A  |   | 1.76<br>1.70             | 1.89<br>1.89               | 2.02<br>2.08             | $V_{DC}$<br>$V_{DC}$    |
| Stability vs Temperature  |   |                          | $\pm 60$                   |                          | ppm/ $^\circ\text{C}$   |
| Stability vs Time, 1000 Hours   |   |                          | $\pm 0.1$                  |                          | %                       |
| <b>LOGIC OUTPUT (Pin 3)</b>   |   |                          |                            |                          |                         |
| $V_{SAT}$   | $I=5\text{ mA}$<br>$I=3.2\text{ mA}$ (2 TTL Loads), $T_{MIN} \leq T_A \leq T_{MAX}$ |                          | 0.15<br>0.10<br>$\pm 0.05$ | 0.50<br>0.40<br>1.0      | V<br>V<br>$\mu\text{A}$ |
| <b>SUPPLY CURRENT</b>   |   |                          |                            |                          |                         |
| LM231, LM231A<br>LM331, LM331A  | $V_S=5\text{V}$<br>$V_S=40\text{V}$<br>$V_S=5\text{V}$<br>$V_S=40\text{V}$          | 2.0<br>2.5<br>1.5<br>2.0 | 3.0<br>4.0<br>3.0<br>4.0   | 4.0<br>6.0<br>6.0<br>8.0 | mA                      |

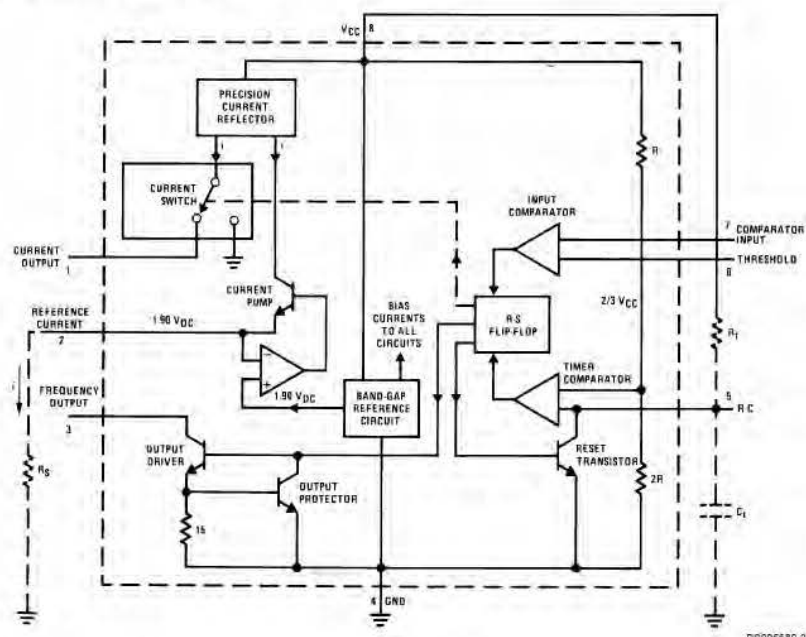
Note 1: Absolute Maximum Ratings indicate limits beyond which damage to the device may occur. DC and AC electrical specifications do not apply when operating the device beyond its specified operating conditions.

Note 2: All specifications apply in the circuit of Figure 4, with  $4.0\text{V} \leq V_S \leq 40\text{V}$ , unless otherwise noted.

Note 3: Nonlinearity is defined as the deviation of  $f_{OUT}$  from  $V_{IN} \times (10\text{ kHz}/10\text{ V}_{DC})$  when the circuit has been trimmed for zero error at 10 Hz and at 10 kHz, over the frequency range 1 Hz to 11 kHz. For the timing capacitor,  $C_T$ , use NPO ceramic, Teflon®, or polystyrene.

Note 4: Human body model, 100 pF discharged through a 1.5 k $\Omega$  resistor.

## Functional Block Diagram



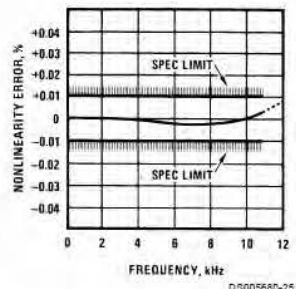
Pin numbers apply to 8-pin packages only.

FIGURE 2.

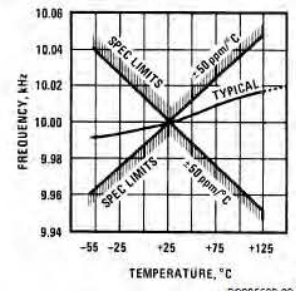
## Typical Performance Characteristics

(All electrical characteristics apply for the circuit of *Figure 4*, unless otherwise noted.)

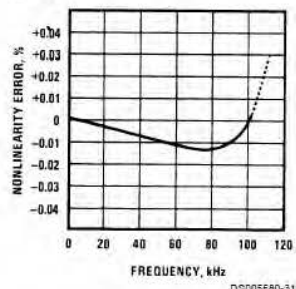
**Nonlinearity Error  
as Precision V-to-F  
Converter (*Figure 4*)**



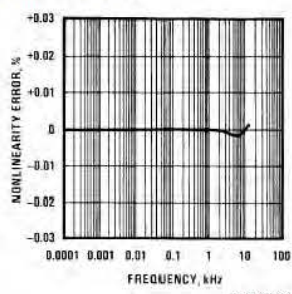
**Frequency vs Temperature**



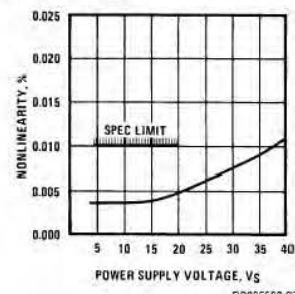
**100 kHz Nonlinearity Error  
(*Figure 5*)**



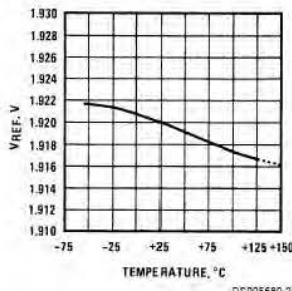
**Nonlinearity Error**



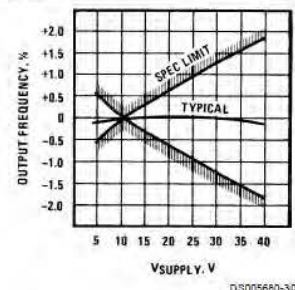
**Nonlinearity Error vs Power Supply Voltage**



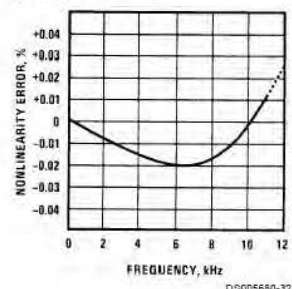
**$V_{REF}$  vs Temperature**



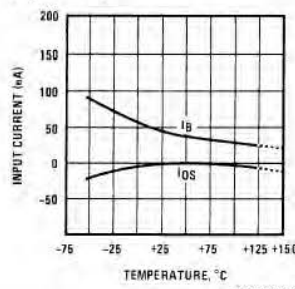
**Output Frequency vs  
 $V_{SUPPLY}$**



**Nonlinearity Error  
(*Figure 1*)**

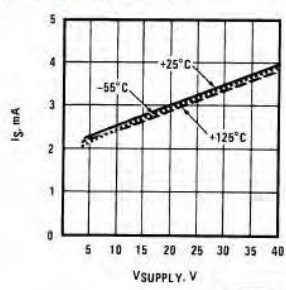


**Input Current (Pins 6,7) vs  
Temperature**



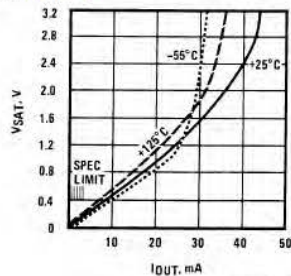
## Typical Performance Characteristics (Continued)

Power Drain vs V<sub>SUPPLY</sub>



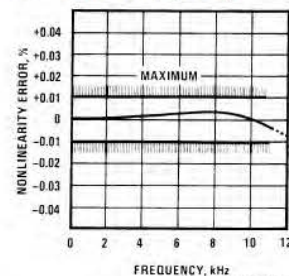
DS005680-34

Output Saturation Voltage vs I<sub>OUT</sub> (Pin 3)



DS005680-35

Nonlinearity Error, Precision F-to-V Converter (Figure 7)



DS005680-36

## Typical Applications

### PRINCIPLES OF OPERATION OF A SIMPLIFIED VOLTAGE-TO-FREQUENCY CONVERTER

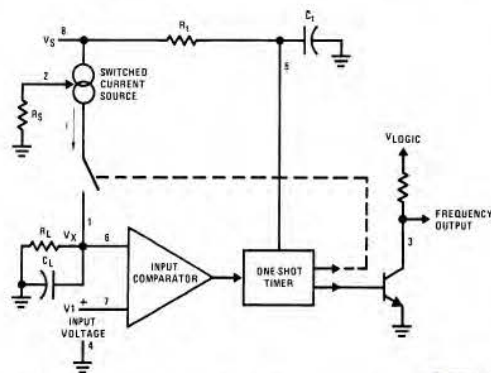
The LM231/331 are monolithic circuits designed for accuracy and versatile operation when applied as voltage-to-frequency (V-to-F) converters or as frequency-to-voltage (F-to-V) converters. A simplified block diagram of the LM231/331 is shown in Figure 3 and consists of a switched current source, input comparator, and 1-shot timer.

The operation of these blocks is best understood by going through the operating cycle of the basic V-to-F converter, Figure 3, which consists of the simplified block diagram of the LM231/331 and the various resistors and capacitors connected to it.

The voltage comparator compares a positive input voltage, V<sub>1</sub>, at pin 7 to the voltage, V<sub>x</sub>, at pin 6. If V<sub>1</sub> is greater, the comparator will trigger the 1-shot timer. The output of the timer will turn ON both the frequency output transistor and the switched current source for a period t=1.1 R<sub>t</sub>C<sub>t</sub>. During this period, the current i will flow out of the switched current source and provide a fixed amount of charge, Q=i x t, into the capacitor, C<sub>L</sub>. This will normally charge V<sub>x</sub> up to a higher level than V<sub>1</sub>. At the end of the timing period, the current i will turn OFF, and the timer will reset itself.

Now there is no current flowing from pin 1, and the capacitor C<sub>L</sub> will be gradually discharged by R<sub>L</sub> until V<sub>x</sub> falls to the level of V<sub>1</sub>. Then the comparator will trigger the timer and start another cycle.

The current flowing into C<sub>L</sub> is exactly I<sub>AVE</sub> = i x (1.1xR<sub>t</sub>C<sub>t</sub>) x f, and the current flowing out of C<sub>L</sub> is exactly V<sub>x</sub>/R<sub>L</sub> ≈ V<sub>IN</sub>/R<sub>L</sub>. If V<sub>IN</sub> is doubled, the frequency will double to maintain this balance. Even a simple V-to-F converter can provide a frequency precisely proportional to its input voltage over a wide range of frequencies.



DS005680-4

FIGURE 3. Simplified Block Diagram of Stand-Alone Voltage-to-Frequency Converter and External Components

### DETAIL OF OPERATION, FUNCTIONAL BLOCK DIAGRAM (Figure 2)

The block diagram shows a band gap reference which provides a stable 1.9 V<sub>DC</sub> output. This 1.9 V<sub>DC</sub> is well regulated over a V<sub>S</sub> range of 3.9V to 40V. It also has a flat, low temperature coefficient, and typically changes less than 1/2% over a 100°C temperature change.

The current pump circuit forces the voltage at pin 2 to be at 1.9V, and causes a current i=1.90V/R<sub>S</sub> to flow. For R<sub>S</sub>=14k, i=135 μA. The precision current reflector provides a current equal to i to the current switch. The current switch switches the current to pin 1 or to ground depending on the state of the R<sub>S</sub> flip-flop.

The timing function consists of an R<sub>S</sub> flip-flop, and a timer comparator connected to the external R<sub>t</sub>C<sub>t</sub> network. When the input comparator detects a voltage at pin 7 higher than pin 6, it sets the R<sub>S</sub> flip-flop which turns ON the current switch and the output driver transistor. When the voltage at pin 5 rises to 2/3 V<sub>CC</sub>, the timer comparator causes the R<sub>S</sub> flip-flop to reset. The reset transistor is then turned ON and the current switch is turned OFF.

However, if the input comparator still detects pin 7 higher than pin 6 when pin 5 crosses 2/3 V<sub>CC</sub>, the flip-flop will not be reset, and the current at pin 1 will continue to flow, in its attempt to make the voltage at pin 6 higher than pin 7. This

## Typical Applications (Continued)

condition will usually apply under start-up conditions or in the case of an overload voltage at signal input. It should be noted that during this sort of overload, the output frequency will be 0; as soon as the signal is restored to the working range, the output frequency will be resumed.

The output driver transistor acts to saturate pin 3 with an ON resistance of about  $50\Omega$ . In case of overvoltage, the output current is actively limited to less than 50 mA.

The voltage at pin 2 is regulated at  $1.90 \text{ V}_{\text{DC}}$  for all values of  $i$  between  $10 \mu\text{A}$  to  $500 \mu\text{A}$ . It can be used as a voltage reference for other components, but care must be taken to ensure that current is not taken from it which could reduce the accuracy of the converter.

### PRINCIPLES OF OPERATION OF BASIC VOLTAGE-TO-FREQUENCY CONVERTER (Figure 1)

The simple stand-alone V-to-F converter shown in *Figure 1* includes all the basic circuitry of *Figure 3* plus a few components for improved performance.

A resistor,  $R_{\text{IN}} = 100 \text{ k}\Omega \pm 10\%$ , has been added in the path to pin 7, so that the bias current at pin 7 ( $-80 \text{ nA}$  typical) will cancel the effect of the bias current at pin 6 and help provide minimum frequency offset.

The resistance  $R_S$  at pin 2 is made up of a  $12 \text{ k}\Omega$  fixed resistor plus a  $5 \text{ k}\Omega$  (cermet, preferably) gain adjust rheostat. The function of this adjustment is to trim out the gain tolerance of the LM231/331, and the tolerance of  $R_t$ ,  $R_L$  and  $C_t$ .

For best results, all the components should be stable low-temperature-coefficient components, such as metal-film resistors. The capacitor should have low dielectric absorption; depending on the temperature characteristics desired, NPO ceramic, polystyrene, Teflon or polypropylene are best suited.

A capacitor  $C_{\text{IN}}$  is added from pin 7 to ground to act as a filter for  $V_{\text{IN}}$ . A value of  $0.01 \mu\text{F}$  to  $0.1 \mu\text{F}$  will be adequate in most cases; however, in cases where better filtering is required, a

$1 \mu\text{F}$  capacitor can be used. When the RC time constants are matched at pin 6 and pin 7, a voltage step at  $V_{\text{IN}}$  will cause a step change in  $f_{\text{OUT}}$ . If  $C_{\text{IN}}$  is much less than  $C_L$ , a step at  $V_{\text{IN}}$  may cause  $f_{\text{OUT}}$  to stop momentarily.

A  $47\Omega$  resistor, in series with the  $1 \mu\text{F}$   $C_L$ , is added to give hysteresis effect which helps the input comparator provide the excellent linearity (0.03% typical).

### DETAIL OF OPERATION OF PRECISION V-TO-F CONVERTER (Figure 4)

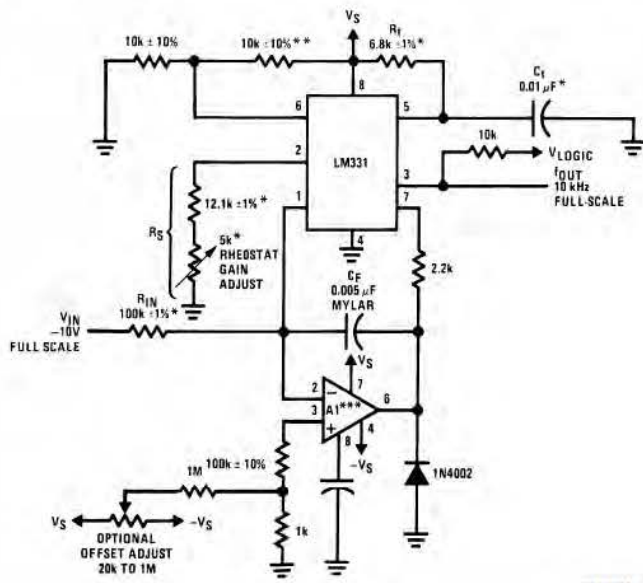
In this circuit, integration is performed by using a conventional operational amplifier and feedback capacitor,  $C_F$ . When the integrator's output crosses the nominal threshold level at pin 6 of the LM231/331, the timing cycle is initiated.

The average current fed into the op amp's summing point (pin 2) is  $i \times (1.1 R_C) \times f$  which is perfectly balanced with  $-V_{\text{IN}}/R_{\text{IN}}$ . In this circuit, the voltage offset of the LM231/331 input comparator does not affect the offset or accuracy of the V-to-F converter as it does in the stand-alone V-to-F converter; nor does the LM231/331 bias current or offset current. Instead, the offset voltage and offset current of the operational amplifier are the only limits on how small the signal can be accurately converted. Since op amps with voltage offset well below 1 mV and offset currents well below 2 nA are available at low cost, this circuit is recommended for best accuracy for small signals. This circuit also responds immediately to any change of input signal (which a stand-alone circuit does not) so that the output frequency will be an accurate representation of  $V_{\text{IN}}$ , as quickly as 2 output pulses' spacing can be measured.

In the precision mode, excellent linearity is obtained because the current source (pin 1) is always at ground potential and that voltage does not vary with  $V_{\text{IN}}$  or  $f_{\text{OUT}}$ . (In the stand-alone V-to-F converter, a major cause of non-linearity is the output impedance at pin 1 which causes  $i$  to change as a function of  $V_{\text{IN}}$ .)

The circuit of *Figure 5* operates in the same way as *Figure 4*, but with the necessary changes for high speed operation.

## Typical Applications (Continued)



0900568C-5

$$f_{OUT} = \frac{-V_{IN}}{2.09 V} \cdot \frac{R_S}{R_{IN}} \cdot \frac{1}{R_f C_t}$$

\*Use stable components with low temperature coefficients. See Typical Applications section.

\*\*This resistor can be 5 kΩ or 10 kΩ for  $V_S$ =8V to 22V, but must be 10 kΩ for  $V_S$ =4.5V to 8V.

\*\*\*Use low offset voltage and low offset current op amps for A1; recommended type LF411A.

FIGURE 4. Standard Test Circuit and Applications Circuit, Precision Voltage-to-Frequency Converter

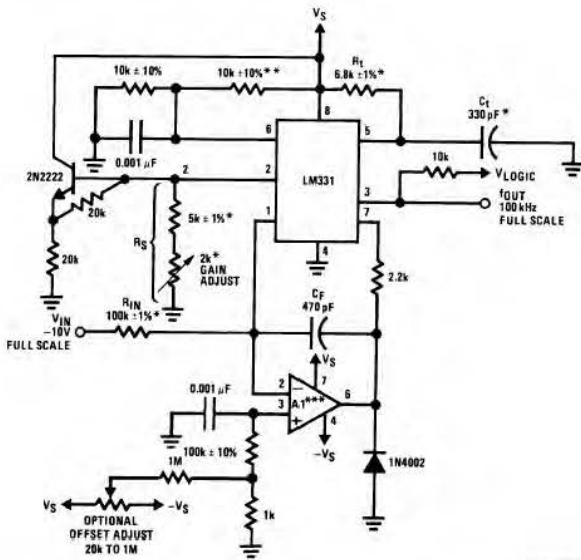
## **Typical Applications** (Continued)

## DETAILS OF OPERATION, FREQUENCY-TO-VOLTAGE CONVERTERS (Figure 6 and Figure 7)

In these applications, a pulse input at  $f_{IN}$  is differentiated by a C-R network and the negative-going edge at pin 6 causes the input comparator to trigger the timer circuit. Just as with a V-to-F converter, the average current flowing out of pin 1 is  $I_{AVERAGE} = i \times (1.1 R_C C_0) \times f$ .

In the simple circuit of Figure 6, this current is filtered in the network  $R_L = 100 \text{ k}\Omega$  and  $1 \mu\text{F}$ . The ripple will be less than 10 mV peak, but the response will be slow, with a 0.1 second time constant, and settling of 0.7 second to 0.1% accuracy.

In the precision circuit, an operational amplifier provides a buffered output and also acts as a 2-pole filter. The ripple will be less than 5 mV peak for all frequencies above 1 kHz, and the response time will be much quicker than in *Figure 6*. However, for input frequencies below 200 Hz, this circuit will have worse ripple than *Figure 6*. The engineering of the filter time-constants to get adequate response and small enough ripple simply requires a study of the compromises to be made. Inherently, V-to-F converter response can be fast, but F-to-V response can not.



\*Use stable components with low temperature coefficients.

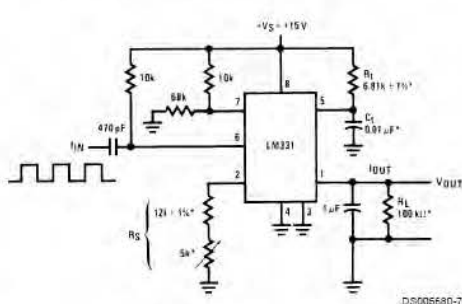
See Typical Applications section.

**\*\***This resistor can be 5 k $\Omega$  or 10 k $\Omega$  for V<sub>S</sub>=8V to 22V, but must be 10 k $\Omega$  for V<sub>S</sub>=4.5V to 8V.

\*\*\*Use low offset voltage and low offset current op amps for A1: recommended types LF411A or LF356.

**FIGURE 5.** Precision Voltage-to-Frequency Converter,  
100 kHz Full-Scale,  $\pm 0.03\%$  Non-Linearity

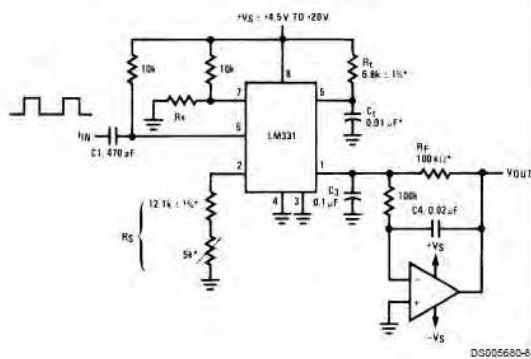
## Typical Applications (Continued)



$$V_{OUT} = f_{IN} \times 2.09V \times \frac{R_L}{R_S} \times (R_t C_l)$$

\*Use stable components with low temperature coefficients.

**FIGURE 6. Simple Frequency-to-Voltage Converter,  
10 kHz Full-Scale,  $\pm 0.06\%$  Non-Linearity**



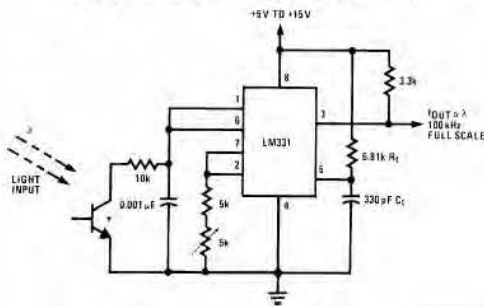
$$V_{OUT} = -f_{IN} \times 2.09V \times \frac{R_F}{R_S} \times (R_t C_l)$$

$$\text{SELECT } R_x = \frac{(V_S - 2V)}{0.2 \text{ mA}}$$

\*Use stable components with low temperature coefficients.

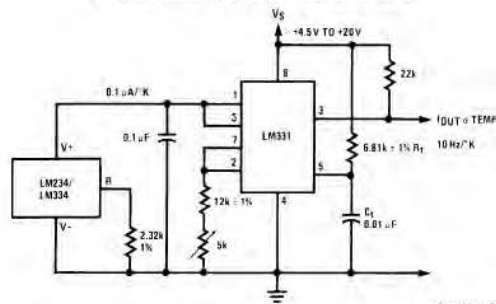
**FIGURE 7. Precision Frequency-to-Voltage Converter,  
10 kHz Full-Scale with 2-Pole Filter,  $\pm 0.01\%$   
Non-Linearity Maximum**

### Light Intensity to Frequency Converter



\*L14F-1, L14G-1 or L14H-1, photo transistor (General Electric Co.) or similar

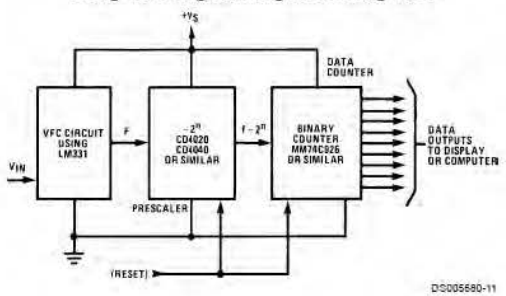
### Temperature to Frequency Converter



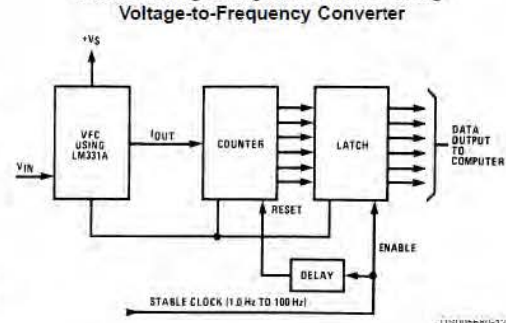
DS005680-10

## Typical Applications (Continued)

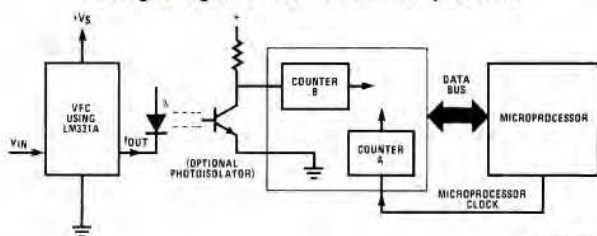
**Long-Term Digital Integrator Using VFC**



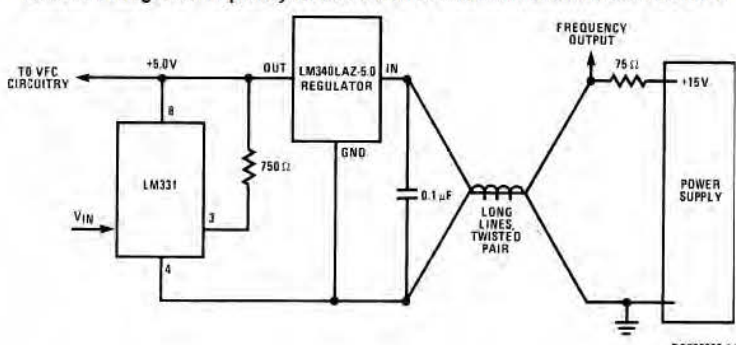
**Basic Analog-to-Digital Converter Using Voltage-to-Frequency Converter**



**Analog-to-Digital Converter with Microprocessor**

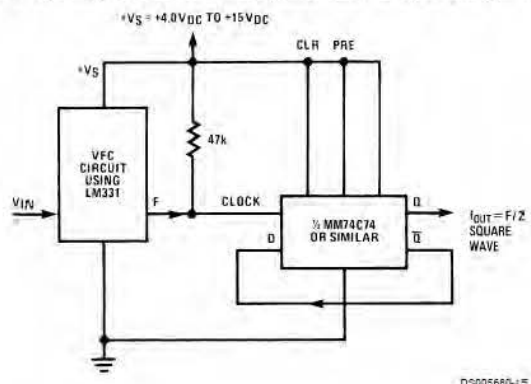


**Remote Voltage-to-Frequency Converter with 2-Wire Transmitter and Receiver**



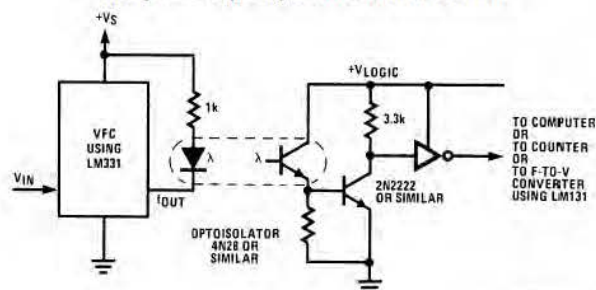
## Typical Applications (Continued)

Voltage-to-Frequency Converter with Square-Wave Output Using  $\div 2$  Flip-Flop



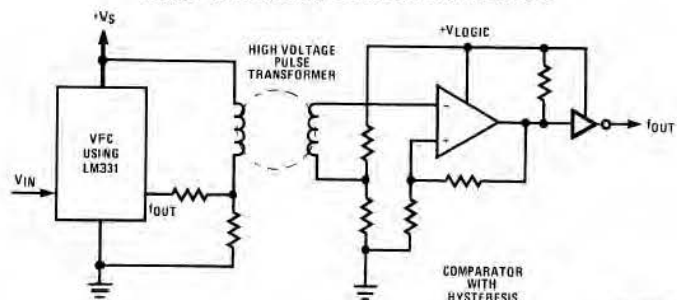
DS005660-1E

Voltage-to-Frequency Converter with Isolators



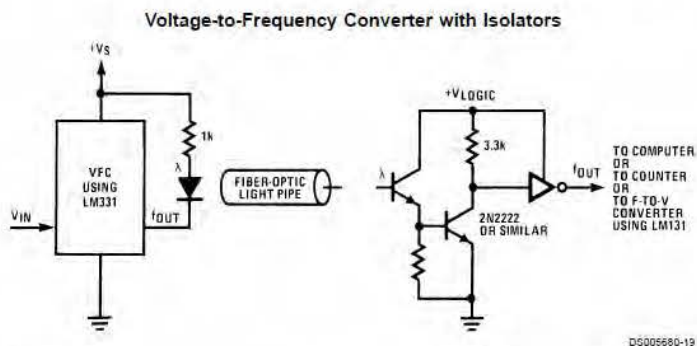
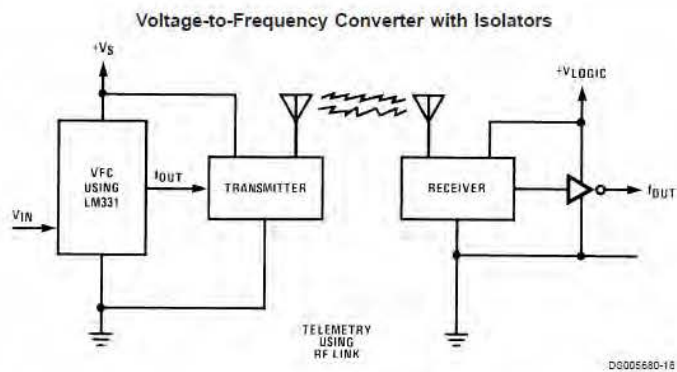
DS005660-16

Voltage-to-Frequency Converter with Isolators

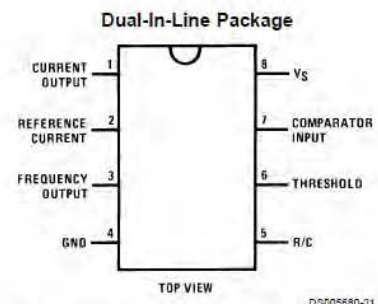


DS005660-17

## Typical Applications (Continued)

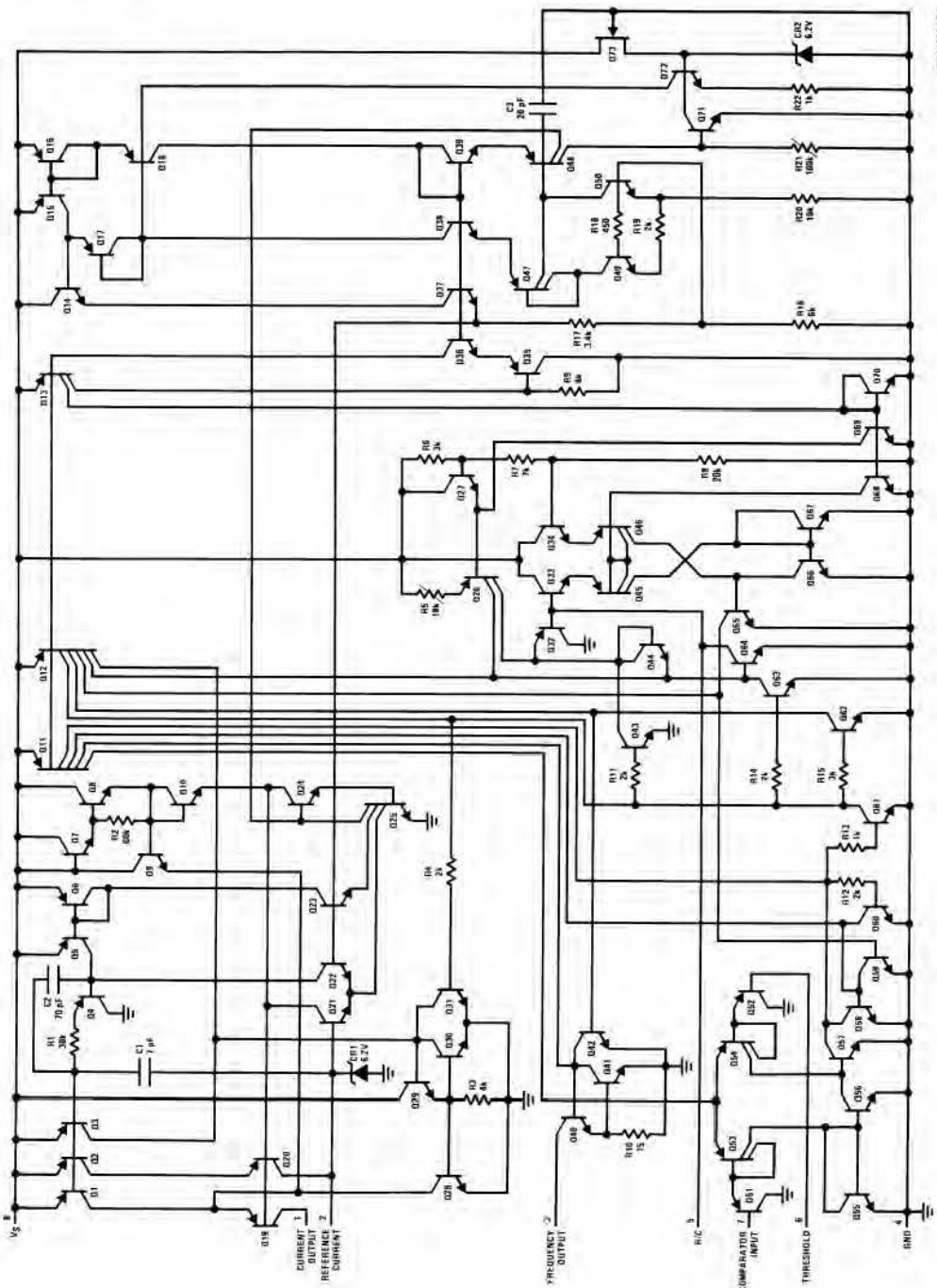


## Connection Diagram



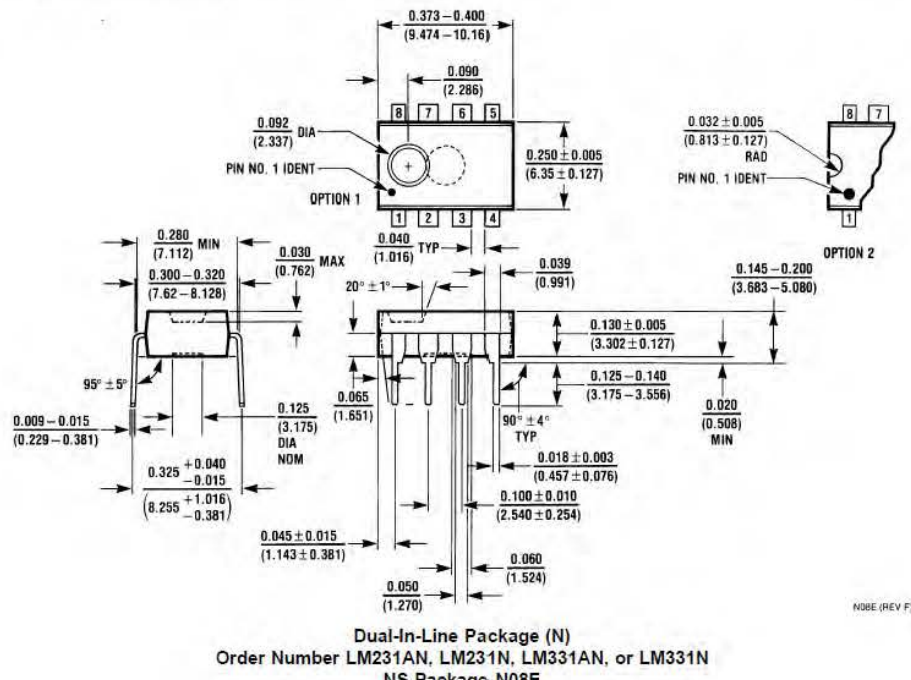
Order Number LM231AN, LM231N, LM331AN,  
or LM331N  
See NS Package Number N08E

## Schematic Diagram



# LM231A/LM231/LM331A/LM331 Precision Voltage-to-Frequency Converters

## Physical Dimensions inches (millimeters) unless otherwise noted



### LIFE SUPPORT POLICY

NATIONAL'S PRODUCTS ARE NOT AUTHORIZED FOR USE AS CRITICAL COMPONENTS IN LIFE SUPPORT DEVICES OR SYSTEMS WITHOUT THE EXPRESS WRITTEN APPROVAL OF THE PRESIDENT AND GENERAL COUNSEL OF NATIONAL SEMICONDUCTOR CORPORATION. As used herein:

1. Life support devices or systems are devices or systems which, (a) are intended for surgical implant into the body, or (b) support or sustain life, and whose failure to perform when properly used in accordance with instructions for use provided in the labeling, can be reasonably expected to result in a significant injury to the user.
2. A critical component is any component of a life support device or system whose failure to perform can be reasonably expected to cause the failure of the life support device or system, or to affect its safety or effectiveness.

**N** National Semiconductor  
Corporation  
Americas  
Tel: 1-800-272-9959  
Fax: 1-800-737-7018  
Email: support@nsc.com  
[www.national.com](http://www.national.com)

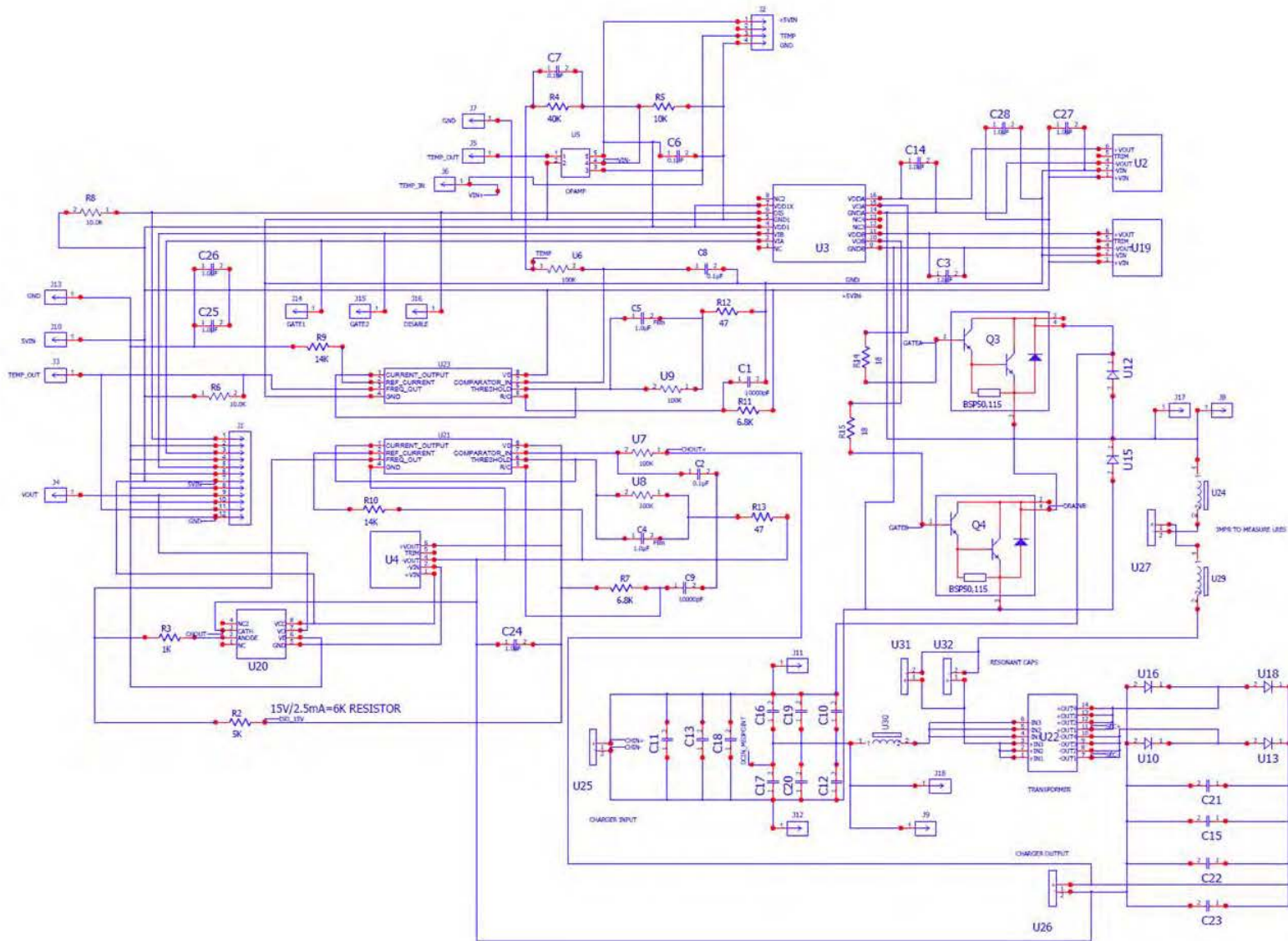
National Semiconductor  
Europe  
Fax: +49 (0) 1 80-530 85 86  
Email: europe.support@nsc.com  
Deutsch Tel: +49 (0) 1 80-530 85 65  
English Tel: +49 (0) 1 80-532 78 32  
Français Tel: +49 (0) 1 80-532 93 58  
Italiano Tel: +49 (0) 1 80-534 16 80

National Semiconductor  
Asia Pacific Customer  
Response Group  
Tel: 65-2544466  
Fax: 65-2504466  
Email: sea.support@nsc.com

National Semiconductor  
Japan Ltd.  
Tel: 81-3-5639-7560  
Fax: 81-3-5639-7507

National does not assume any responsibility for use of any circuitry described, no circuit patent licenses are implied and National reserves the right at any time without notice to change said circuitry and specifications.

## APPENDIX D. SLR CONVERTER ONE LINE DIAGRAM



THIS PAGE INTENTIONALLY LEFT BLANK

## LIST OF REFERENCES

- [1] Office of Naval Research. (2012, June 22). *Shore energy management* [Online]. Available: <http://greenfleet.dodlive.mil/files/2012/07/OPNAVINST-4100.5E.pdf>
- [2] Electricity Storage Association. *Technology comparisons* [Online]. Available: [http://www.electricitystorage.org/technology/tech\\_archive/technology\\_comparisons](http://www.electricitystorage.org/technology/tech_archive/technology_comparisons)
- [3] G. Oriti, A. L. Julian, and N. J. Peck, “Power electronics enabled energy management systems,” in *Proc. of IEEE Appl. Power Electron. Conference (APEC)*, Long Beach, CA, Mar. 2013, pp. 3224–3231.
- [4] R. L. Kelly, A. L. Julian, and G. Oriti, “Reducing fuel consumption in a forward operating base using an energy management System,” in *Proc. of the IEEE 5th Energy Conversion Conference and Expo (ECCE)*, Denver, CO, Sept. 2013, pp 1330–1336.
- [5] M. Yilmaz and P. T. Krein, “Review of battery charger topologies, charging power levels, and infrastructure for plug-in electric and hybrid vehicles,” in *IEEE Trans. Edu.*, vol. 28, no. 5, pp. 2151–2169, May 2013.
- [6] Y. H. Hsieh, T. J. Liang, S. M. Chen, W. Y. Horng, and Y. Y. Chung, “A novel high-efficiency compact-size low-cost balancing method for series-connected battery applications,” *IEEE Trans. Edu.*, vol. 28, no. 12, pp. 5927–5939, Dec. 2013.
- [7] National Semiconductor, “Precision voltage-to-frequency converters,” LM231A/LM231/LM331A/LM331 datasheet, June 1999. [Online]. Available: <http://ee-classes.usc.edu/ee459/library/datasheets/LM331.pdf>
- [8] Yuasa, “NP-series-valve regulated lead acid battery,” NP12–12 datasheet, Mar. 2011. [Online]. Available: [http://www.yuasaeurope.com/images/uploads/eu/downloads/datasheets/NP/NP12-12\\_English.pdf](http://www.yuasaeurope.com/images/uploads/eu/downloads/datasheets/NP/NP12-12_English.pdf)
- [9] Clemson University. *Linear regression and Excel* [Online]. Available: <http://www.clemson.edu/ces/phoenix/tutorials/excel/regression.html>
- [10] J. Stewart, *Calculus Early Transcendentals* (7th ed.). Belmont CA: Brooks/Cole, 2010, pp. 371–382.

- [11] A. L. Julian, G. Oriti, and M. E. Pfender, “SLR converter design for multi-cell battery charging,” in *Proc. of the IEEE 5th Energy Conversion Conference and Expo (ECCE)*, Denver, CO, Sept. 2013, pp. 743–748.
- [12] M. E. Pfender, “Simulating and testing a DC-DC half bridge SLR converter,” M.S. thesis, Dept. of Elect. and Comput. Eng., Naval Postgraduate School, Monterey, CA, 2013.
- [13] *System Generator for DSP Getting Started Guide*, version 11.4, Xilinx Inc., San Jose, CA, Dec. 2009, p. 30.
- [14] *Virtex-4<sup>TM</sup> LC Rev2 Development Board User’s Guide Version*, version 2.0, Memec Group Ltd., Stevenage, UK, May 2005, p. 8.

## **INITIAL DISTRIBUTION LIST**

1. Defense Technical Information Center  
Ft. Belvoir, Virginia
2. Dudley Knox Library  
Naval Postgraduate School  
Monterey, California